



Doubly-resonant two-photon-absorption-induced four-wave mixing in $\text{Tb}(\text{OH})_3$ and LiTbF_4
by David Adams Ender

A thesis submitted in partial fulfillment of the requirements for the degree of DOCTOR OF
PHILOSOPHY in Physics
Montana State University
© Copyright by David Adams Ender (1982)

Abstract:

Doubly-resonant two-photon-absorption-induced four-wave mixing has been observed for the first time in a rare earth insulator. The generation of the nonlinear signal exhibits strong intermediate and two-photon resonances in crystalline $\text{Tb}(\text{OH})_3$ and LiTbF_4 . This provides a novel method for high resolution measurements of intermediate $4f^n$ configurations and excited configurations of rare earth ions.

The intermediate resonance showed spectral line narrowing up to ten times narrower than the corresponding inhomogeneously broadened absorption. In LiTbF_4 , laser-limited line widths were obtained and in $\text{Tb}(\text{OH})_3$, a homogeneous limit corresponding to $T_2 = 50$ psec may have been reached. The qualitative behavior of the narrowing is explained by the dispersion of the anomalous index of refraction and its effect on phase matching. Direct measurement of the anomalous dispersion was made to test the model. Results indicate nonlinear contributions to the refractive index may have been present.

The two-photon resonance in $\text{Tb}(\text{OH})_3$ was measured to be a 230 cm^{-1} wide crystal field component of the broad $4f^n 5d$ excited configuration. Thus high resolution UV spectroscopy with tunable visible lasers is demonstrated.

Applications are discussed including the extraction of homogeneous line widths from inhomogeneously broadened spectra, coherent transient measurements, and UV and VUV spectroscopy. The latter uses different selection rules than linear absorption methods and allows study of transitions between excited states.

DOUBLY-RESONANT TWO-PHOTON-ABSORPTION-INDUCED FOUR-WAVE

MIXING IN $Tb(OH)_3$ AND $LiTbF_4$

by

DAVID ADAMS ENDER

A thesis submitted in partial fulfillment
of the requirements for the degree

of

DOCTOR OF PHILOSOPHY

in

Physics

Approved:

R. L. Cone
Chairperson, Graduate Committee

David Stevenson
Head, Major Department

Michael Malone
Graduate Dean

MONTANA STATE UNIVERSITY
Bozeman, Montana

August, 1982

ACKNOWLEDGEMENTS

The author wishes to acknowledge the contributions of several people to the preparation of this thesis. Foremost has been the encouragement and patience of his adviser, Dr. R. L. Cone, who initiated the project and whose scientific knowledge and guidance helped bring it to completion.

Thanks also are due to Mr. Michael Otteson and Ms. Paula Fisher for help in building equipment and computerization; to Mr. Tony Knick, Mr. Al Beldring, and Mr. Mark Baldwin in building apparatus; to Mr. Milt Jaehnig for his help in leak detection; to Dr. Roy Wiegand for his successful efforts at keeping the liquid nitrogen machine working; to Dr. Douglas Jones for the laser trigger and delay unit; and to Mr. Mark Ritter for sample preparation.

The author also wishes to thank the members of his committee for their encouragement and suggestions.

He thanks the National Science Foundation for its support as well as the Research Corporation.

Finally, he wishes to extend heartfelt thanks to his parents for their encouragement over the years.

TABLE OF CONTENTS

Chapter		Page
	Vita.	ii
	Acknowledgements.	iii
	Table of Contents	iv
	List of Tables.	v
	List of Figures	vi
	Abstract.	viii
1	HISTORY AND SURVEY.	1
	History	2
	Nonlinear Spectroscopy.	6
	Frequency Domain Spectroscopy	7
	Time Domain Spectroscopy.	9
2	THEORY OF FOUR-WAVE MIXING IN SOLIDS.	11
	Four-Wave Mixing.	11
	Materials	29
	Spectral Line Broadening.	36
3	APPARATUS AND SAMPLES	40
	System Optics	40
	Lasers.	44
	Dewars and Dewar Optics	45
	Electronics	45
	Samples	46
4	RESULTS AND DISCUSSION.	48
	Nature of Signal.	48
	Line Narrowing.	58
	Applications.	75
5	CONCLUSIONS	78
	APPENDICES.	83
	Appendix I.	84
	Appendix II	94
	Appendix III.	100
	Appendix IV	103
	REFERENCES.	106

LIST OF TABLES

Table		Page
2.1	Summary of Relevant Equations	23
2.2	Tb(OH) ₃ Allowed Transitions	35
2.3	LiTbF ₄ Allowed Transitions	35
4.1	⁷ F _J Energy Levels	53

LIST OF FIGURES

Figure		Page
1.1	Four-wave mixing signal shown with absorption.	3
1.2	Second harmonic generation.	4
2.1	Energy level diagram used in $\chi^{(3)}$	16
2.2	$\text{Sinc}^2 (\Delta k L/2)$ vs. $\omega_1/2\pi$	25
2.3	Phase matching diagrams	26
3.1	Optical system used in FWM experiments.	42
4.1	Fluorescent excitation spectrum shown with absorption	49
4.2	Log (signal power) vs. log (input power).	51
4.3	Broad linear UV absorption band $\text{Tb}(\text{OH})_3$	56
4.4	Resolved $4f^7 5d$ crystal field component using FWM	57
4.5	FWM signal in LiTbF_4 for different crossing angles	60
4.6	White-light absorption coefficient and index of refraction vs. ω_1	63
4.7	Dependence of FWM signal on ω_3	64
4.8	FWM signal in $\text{Tb}(\text{OH})_3$ for different crossing angles	66
4.9	Computer simulation of equation (4.1)	68
4.10	Computer simulation of equation (4.1) with Δn increased by 3.8.	69

List of Figures, Continued

Figure		Page
4.11	Computer simulation of equation (4.1) with Δn increased 35 times.	70
4.12	Gaussian profile fitted to absorption coefficient $\alpha(\omega_1)$	71
4.13	Lorentzian profile fitted to absorption coefficient $\alpha(\omega_1)$	71
Appendix Figures		
I.1	Pulse sequence-transient case	87
I.2	Energy level diagram-transient case	88
II.1	Beam deviation through prism.	96
II.2	Experimental set-up: index experiment.	99

Abstract

Doubly-resonant two-photon-absorption-induced four-wave mixing has been observed for the first time in a rare earth insulator. The generation of the nonlinear signal exhibits strong intermediate and two-photon resonances in crystalline $\text{Tb}(\text{OH})_3$ and LiTbF_4 . This provides a novel method for high resolution measurements of intermediate $4f^n$ configurations and excited configurations of rare earth ions.

The intermediate resonance showed spectral line narrowing up to ten times narrower than the corresponding inhomogeneously broadened absorption. In LiTbF_4 , laser-limited line widths were obtained and in $\text{Tb}(\text{OH})_3$, a homogeneous limit corresponding to $T_2 = 50$ psec may have been reached. The qualitative behavior of the narrowing is explained by the dispersion of the anomalous index of refraction and its effect on phase matching. Direct measurement of the anomalous dispersion was made to test the model. Results indicate nonlinear contributions to the refractive index may have been present.

The two-photon resonance in $\text{Tb}(\text{OH})_3$ was measured to be a 230 cm^{-1} wide crystal field component of the broad $4f^n 5d$ excited configuration. Thus high resolution UV spectroscopy with tunable visible lasers is demonstrated.

Applications are discussed including the extraction of homogeneous line widths from inhomogeneously broadened spectra, coherent transient measurements, and UV and VUV spectroscopy. The latter uses different selection rules than linear absorption methods and allows study of transitions between excited states.

Chapter 1

HISTORY AND SURVEY

The propagation of an intense laser beam in matter often generates light at frequencies different than that of the laser itself. Several laser beams can create light at a mixture of frequencies. In addition, such light mixing can interact coherently with the medium of propagation as well as exhibit resonant behavior. The branch of optics describing these phenomena is called nonlinear optics.

The subject of this thesis deals with the first observation of two nonlinear optical effects: (1) doubly-resonant two-photon absorption-induced four-wave mixing (TPAFWM) in rare earth insulators (specifically $\text{Tb}(\text{OH})_3$ and LiTbF_4), and (2) phase matching induced line narrowing.

The initial observation of the TPAFWM signal was made by Rufus Cone and Joel Friedman at Bell Telephone Laboratories, Murray Hill.¹ Light at $\omega_4 = \omega_1 + \omega_2 - \omega_3$ was observed upon application of beams at frequencies ω_1, ω_2 and ω_3 . The ω_4 beam intensity exhibits resonant behavior as the input beams are tuned relative to transitions of the crystal, making this technique highly useful for spectroscopy.

The surprising thing found at Murray Hill was the extreme spectral narrowing exhibited by the ω_4 signal

inside the corresponding ω_1 absorption line shape (see Figure 1.1). Subsequent observations at Montana State University showed that the narrowed line could be driven from one side of the ω_1 resonance to the other upon variation of the beam crossing angles.² This report confirms this as a TPAFWM process and explains the nature of the narrowing, the peculiar shape, and its spectral motion. Utilization of this process as a spectroscopic tool will also be discussed.³

History

The field of nonlinear optics was ushered in by the classic experiment done in July of 1961 by Franken, Hill, Peters, and Weinreich⁴ in which second harmonic generation (SHG) was first measured. Light from a ruby laser at 6943 Å was focused into a crystalline quartz sample as in Figure 1.2. The resultant beam was spectrally analyzed yielding photographic plates showing not only light at 6943 Å but also a faint spot at 3471.5 Å. The conversion efficiency was 10^{-8} . Today, efficiencies close to one are routinely achieved.⁵

Nonlinear optical effects arise from higher order terms of the induced polarization of a medium which is

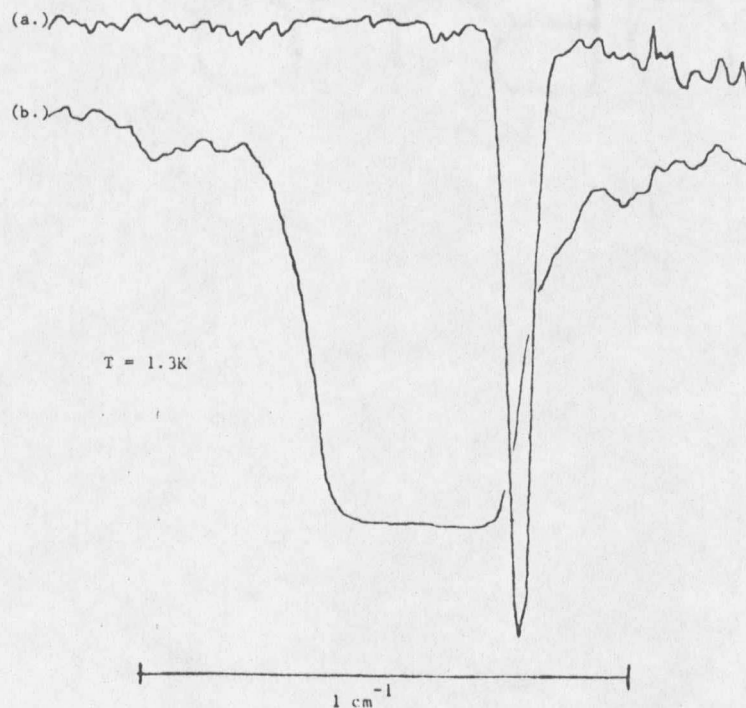


Figure 1.1. (a.) Four-wave mixing signal, and (b.) corresponding absorption for the ${}^5D_4\Gamma_1$ state of LiTbF_4 . $\omega_3 = 17422 \text{ cm}^{-1}$. Crossing angle $\theta = 1.50^\circ$.

written as an expansion in powers of E/E_{at} :

$$P = \chi E \left(1 + C_1 \frac{E}{E_{\text{at}}} + C_2 \left(\frac{E}{E_{\text{at}}} \right)^2 + \dots \right) \quad (1.1)$$

The C_i are expansion coefficients of order one and $E_{\text{at}} \sim \frac{e}{2a_0} = 1.7 \times 10^7$ statvolts/cm is the typical atomic field an electron sees in a transparent insulator ($a_0 =$ one Bohr radius).

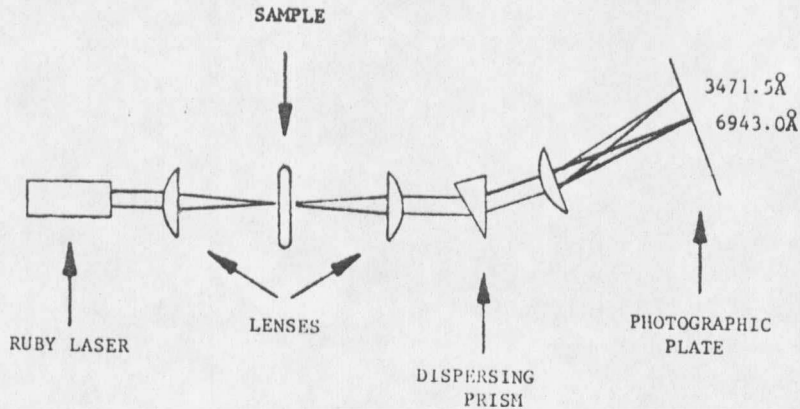


Figure 1.2. Second harmonic generation in crystalline quartz. The ruby laser emits at 6943.0\AA . The sample generates light at 3471.5\AA .

This oscillating polarization acts as a source term in Maxwell's equations generating light at the various frequencies given by a Fourier decomposition of P .

One usually rewrites Equation (1.1) as

$$\vec{P} = \epsilon_0 \chi^{(1)} \cdot \vec{E} + \chi^{(2)} : \vec{E}\vec{E} + \chi^{(3)} : \vec{E}\vec{E}\vec{E} + \dots, \quad (1.2)$$

where the tensor coefficients of the electric field are referred to as the linear ($\chi^{(1)}$) and nonlinear ($\chi^{(2)}$, $\chi^{(3)}$, ...) electric susceptibilities of the medium.

We can see immediately that the oscillation of the parent electric field at frequency ω in Franken's SHG

experiment will generate a polarization in the medium oscillating at 2ω for nonzero $\chi^{(2)}$. Likewise, higher order terms will produce other harmonics and for situations involving input waves of distinct frequencies various sum and difference frequencies will be generated. Nonlinear optics is a colorful subject.

Nonlinear effects in the polarization have been studied since the nineteenth century (Pockels and Kerr effects).⁶ However, it wasn't until the advent of the laser in July of 1960 that the ability was obtained to generate light waves intense enough to utilize the higher order terms in the expanded polarization.⁷

Consequently, little motivation existed to develop a global theoretical approach to the many nonlinear optical effects awaiting discovery. The years from 1961 to the present have been spent primarily laying the theoretical framework, fitting new observations into it, and working out the finer details of the theory.

While the future still holds promise for the discovery of new effects, the majority of workers in the field are directing their research more toward device applications⁸ or applications of nonlinear optical spectroscopy. The latter topic is considered important enough that Nicholaas

Bloembergen and Arthur Schawlow won the 1981 Nobel prize in physics for their work in the field.⁹ In particular, it is Bloembergen's work in four-wave mixing that forms the background for this thesis.

Nonlinear Spectroscopy

Several general reviews exist on the field of nonlinear optical spectroscopy. Bloembergen has written several excellent articles on nonlinear optics for which two are exceptionally comprehensive.¹⁰ Hänsch,¹¹ Levenson,¹² and Brewer¹³ each have short topical articles with good reference lists on some of the more important subfields on nonlinear optical spectroscopy. More recent reviews are given by Levenson and Song¹⁴ and Laubereau and Kaiser¹⁵ on coherent Raman spectroscopy and coherent time domain Raman spectroscopy respectively. The former is worthwhile on the basis of its reference list alone.

Nonlinear laser spectroscopy provides information in both frequency and temporal domains. In many cases it offers distinct advantages over linear spectroscopy. These include higher resolution and signal sensitivity. Dynamics of collective excitations, both coherent and incoherent, can be studied, and multiphoton processes enable different

sets of selection rules to be used.

Frequency Domain Spectroscopy

Many methods have been developed for spectroscopy in the frequency domain. Use of the third order susceptibility $\chi^{(3)}$ provides such techniques as stimulated Raman scattering (SRS),^{14,16,17} coherent antistokes Raman spectroscopy (CARS),^{12,14,18} coherent Stokes Raman spectroscopy (CSRS),^{19,20} two-photon-absorption-induced four-wave mixing (TPAFWM),^{21,22,23} and degenerate four-wave mixing (DFWM).^{24,25,26} A chief advantage of these techniques lies in the fact that the output signal is generally separated spatially from the input beams and is of a different frequency. Thus easy signal discrimination is obtained.

The ability to measure homogeneous linewidths inside of inhomogeneously broadened²⁷ spectral lines is a topic of much interest. By measuring the width of the homogeneous line one obtains the associated relaxation time. This provides insight into the dynamics of the excited state. Certain nonlinear techniques can extract this information where linear techniques fail.

One such method, saturation or hole-burning spectroscopy,^{28,29} involves saturating the narrower homogeneous

part of the inhomogeneous line with a strong pump laser, then probing the absorption profile with a weaker probe beam. When the probe frequency comes into the saturated part of the absorption, it is no longer absorbed. Thus, an absorption profile with a "hole" is mapped out. The hole provides a measure of the homogeneous linewidth.

Doppler-free two-photon spectroscopy^{11,30} complements single photon spectroscopy in that it provides spectral information between states of the same parity. It is especially valuable in studying gases where the photon frequencies are Doppler shifted as viewed by molecules traveling with different velocities. This inhomogeneously broadens the transition. By utilizing photons traveling in opposite directions, the first order Doppler shifts cancel yielding nearly homogeneous line shapes in the fluorescence spectrum.

Nonlinear polarization spectroscopy^{11,31,32} is closely related to saturation spectroscopy. However, rather than monitoring the probe's absorption, the polarization is examined. The pump laser induces a birefringence in the sample which changes the polarization of the probe. By placing the sample between crossed polarizers, very high signal-to-noise ratios are possible. When the pump and

probe frequencies differ by a Raman transition, this method is called RIKES (Raman Induced Kerr Effect Spectroscopy).^{12,33}

Time Domain Spectroscopy

Nonlinear spectroscopy can also be applied to the time domain, allowing relaxation rates to be measured directly. This is especially useful in those situations where homogeneous linewidths are too narrow to be measured directly with present lasers. These kinds of measurements are called coherent transient techniques^{13,34} because they involve inducing a coherent state in the system under study, terminating the source of coherence, and finally probing the relaxation as a function of time.

Two kinds of relaxation processes are distinguished. Those processes that act to destroy the induced collective coherence of the atomic dipoles are called transverse processes and have decay time T_2 , while those that depopulate the energy levels are longitudinal processes having decay time T_1 . The terminology is borrowed from nuclear magnetic resonance language because a two-level optical system can be described in terms of the Bloch equations.³⁴

Free induction decay and photon echo experiments

provide means to measure the homogeneous T_2 of inhomogeneously broadened lines.³⁵ Macfarlane and Shelby,³⁶ using a photon echo technique, have been able to measure T_2 of 429 μsec corresponding to a homogeneous linewidth of 760 Hz in $\text{Eu}^{3+}:\text{Y}_2\text{O}_3$. This is the smallest homogeneous linewidth ever measured.

A different approach to measuring relaxation times involves delayed probing of a coherently prepared system. CARS,^{37,38} TPAFWM, and other multi-beam techniques can be used as time domain methods by temporal sequencing of the pulses from different lasers. Induced coherence established by earlier pulses decays away upon pulse termination. Sampling of the remaining coherence as a function of the delay time of a later probe pulse allows T_2 to be measured. In addition, the delayed CARS technique can also be used to measure T_1 .³⁷

The above survey of experimental methods is by no means intended to be complete, but rather is meant to give the reader a flavor for the many ways in which nonlinear optical techniques can be used in spectroscopy. One of the methods mentioned, two-photon-absorption-induced four-wave mixing is the thrust of this thesis.

Chapter 2

THEORY OF FOUR-WAVE MIXING IN SOLIDS

The theory of four-wave mixing (FWM) is presented first in order to provide a framework from which to understand the phenomena observed. Then the relevant properties of the materials under study, namely $Tb(OH)_3$ and $LiTbF_4$, are presented. It should be noted, however, that the line narrowing and spectral selectivity observed is a general effect which needs to be considered in resonant FWM experiments on all materials in condensed states. This will become apparent in Chapter 4.

Four-Wave Mixing

The fitting of new observations into the theoretical framework of nonlinear optics requires examination of the underlying assumptions made. Furthermore, as will be seen, the nonlinear susceptibility is composed of several terms, each describing a different nonlinear process. In order to understand the nature of the signal observed, investigation of the contribution of these terms is necessary. The following treatment, taken from Ducuing and from Bloembergen³⁹, highlights both the assumptions made and relevant terms needed to explain our observations.

Four-wave mixing is treated most suitably using a semiclassical approach which treats the light fields classically and the material quantum mechanically. Because this is a coherent process, phase information is important and is handled quite conveniently by classical fields. This approach is well justified when dealing with large numbers of photons (i.e. for pulse energies $\gg \hbar\omega \sim 4 \times 10^{-19} \text{ J}$) as is the case in our experiments.

The strategy is summarized as follows. We are interested in the interaction of Th^{3+} ions in a crystal with an applied electromagnetic field due to the light. The Hamiltonian is given by $H = H_0 + H'(t)$ where H_0 is the material Hamiltonian. $H'(t)$ is the perturbation due to the applied field. We use H in the equation of motion for ρ , the quantum mechanical density operator, which is solved by an iterative perturbation technique in which ρ is expanded in powers of H' . The macroscopic polarization of the medium due to H' is given by

$$\vec{P} = N \langle \vec{\mu} \rangle = N \text{Trace} (\rho \vec{\mu}) \quad (2.1)$$

where N = the particle density and $\vec{\mu}$ = the atomic electric dipole moment. Substitution of \vec{P} into Maxwell's equations yields the equation of propagation for $\vec{E}_{\text{rad}}(\vec{x}, t)$, the gen-

erated wave in the medium. The FWM signal is one of the Fourier components of this wave.

We begin by writing the electric field of the light wave with four frequency components as

$$\vec{E}(\vec{x}, t) = \sum_{n=1}^4 \vec{E}_{on}(\vec{x}) \exp(i\omega_n t) + \text{c.c.} \quad (2.2)$$

The electric dipole approximation is used in which the wavelength of the exciting radiation is long compared to the size of the atom. The Hamiltonian is written

$$H = H_0 - e\vec{E}(\vec{x}, t) \cdot \vec{x} \quad (2.3)$$

The equation of motion for ρ in the Schrodinger picture is given by

$$i\hbar\dot{\rho} = [H, \rho] + i\hbar\dot{\rho}_{\text{relax}} \quad (2.4)$$

where $\dot{\rho}_{\text{relax}}$ ²² is a phenomenological term included to account for damping of the material resonances. We use basis states $|n\rangle$ in which H_0 is diagonal in writing

$$(\dot{\rho}_{\text{relax}})_{nn'} = -\Gamma_{nn'}\rho_{nn'} \quad (2.5)$$

where $\Gamma_{nn'} = \Gamma_{n'n}$ is the damping constant of the induced dipole moment associated with the states n and n' , and

$$(\dot{\rho}_{\text{relax}})_{nn} = -\sum_{n'} \gamma_{n'n} \rho_{nn} + \sum_{n'} \gamma_{nn'} \rho_{n'n'} \quad (2.6)$$

where $\gamma_{n'n}$ is the transition rate from the state n to n' , $T_2 = (2\pi\Gamma_{nn'})^{-1}$ is the dephasing time, and for a two-level system, $T_1 = (\gamma_{n'n})^{-1}$ is the population relaxation time. (Note that it is common in the literature to use " Γ " for dipole decay and " γ " for population decay.)

Expansion of ρ in increasing powers of $H'(t)$ gives, upon substitution into equation (2.4),

$$i\hbar\dot{\rho}^{(n)} = [H_0, \rho^{(n)}] + i\hbar\dot{\rho}_{\text{relax}}^{(n)} + [H', \rho^{(n-1)}] \quad (2.7)$$

$$\text{where } \rho(t) = \rho^{(0)} + \rho^{(1)} + \rho^{(2)} + \rho^{(3)} + \dots \quad (2.8)$$

and $\rho^{(0)}(t) = \rho(0)$ defined by the initial conditions that $\rho_{nn}(0)$ equals the thermalized occupation probabilities of the states $|n\rangle$ and $\rho_{n'n}(0) = 0$. At low temperatures this can be further simplified by allowing initial occupation of only the ground state. As discussed in Chapter 4, in our system changes in population are ignored so that $\rho_{gg}(t) = \rho_{gg}(0) = 1$. Finally we look at only the steady state response of $\rho(t)$. This is justified for rapid dephasing ($1/\Gamma_{nn} \ll$ laser pulse duration) of all dipole moments, which is expected in the concentrated magnetic compounds

under study.

Using (2.1) with the above assumptions we concentrate on the terms in the polarization oscillating at frequency $\omega_4 = \omega_1 + \omega_2 - \omega_3$. Laser frequencies ω_1 , ω_2 , and ω_3 are chosen for our experiment to match the energy levels as shown in Figure 2.1a.

Defining $\chi^{(3)}$ as in (1.2), we arrive at the following expression^{23,39} for $\chi^{(3)}$ applied to our system

$$\chi_{\mu\alpha\beta\gamma}^{(3)}(\omega_4 = \omega_1 + \omega_2 - \omega_3)_\alpha$$

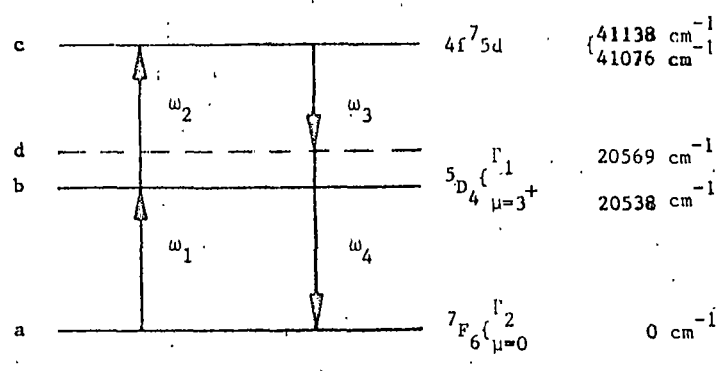
$$\sum_{n=\text{all states}} \frac{\mu_{\alpha,ab} \mu_{\beta,bc} \mu_{\mu,cn} \mu_{\gamma,na} (-\rho_{aa}^{(0)})}{(\omega_{ba} - \omega_1 - i\Gamma_{ba}) (\omega_{ca} - (\omega_1 + \omega_2) - i\Gamma_{ca}) (\omega_{cn} - \omega_4 - i\Gamma_{cn})}$$

$$+ \sum_{n=\text{all states}} \frac{\mu_{\alpha,ab} \mu_{\beta,bc} \mu_{\gamma,cn} \mu_{\mu,na} (\rho_{aa}^{(0)})}{(\omega_{ba} - \omega_1 - i\Gamma_{ba}) (\omega_{ca} - (\omega_1 + \omega_2) - i\Gamma_{ca}) (\omega_{na} - \omega_4 - i\Gamma_{na})} +$$

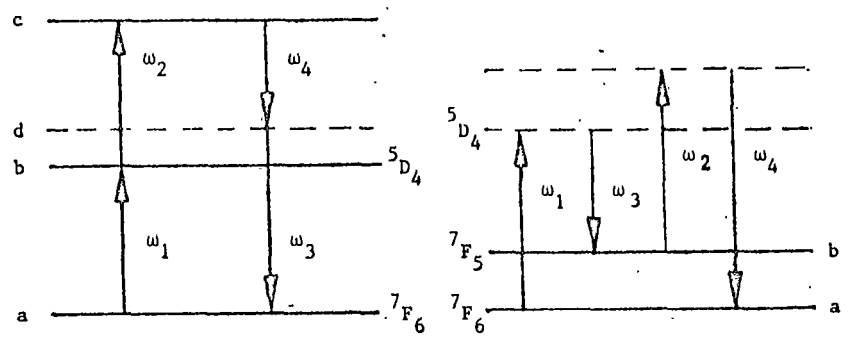
(2.10)

46 other nonresonant (N.R.) terms, where $\omega_{ij} \equiv (E_i - E_j)/\hbar$. Nonresonant terms refer to those terms which are small compared to those shown by choice of the input frequencies ω_1 , ω_2 , and ω_3 .

As discussed in Chapter 4, consideration of Raman contributions such as CARS and CSRS (pronounced "scissors") was necessary. These terms look like¹⁹



(a.) TPA



(b.) TPA

(c.) CARS

Figure 2.1. Energy level diagrams for various terms in $\chi^{(3)}$ ($\omega_4 = \omega_1 + \omega_2 - \omega_3$). Material energy levels used in our experiments are identified for $\begin{cases} \text{LiTbF}_4 \\ \text{Tb(OH)}_3 \end{cases}$ in Figure (a.).

$$\chi^{(3)}(\omega_4) \sim \frac{1}{(\omega_{ba} - (\omega_1 - \omega_3) - i\Gamma_{ba})} \text{ for } \omega_1 > \omega_3 \text{ (CARS)} \quad (2.11)$$

$$\sim \frac{1}{(\omega_{ba} + (\omega_1 - \omega_3) - i\Gamma_{ba})} \text{ for } \omega_1 < \omega_3 \text{ (CSRS)} \quad (2.12)$$

It will be shown later that the signal produced at ω_4 is $\propto |\chi^{(3)}|^2$. Thus interferences can occur between the terms. For this reason it was necessary to know if the Raman terms of (2.11) and (2.12) were contributing resonantly to the signal. We found the ω_4 signal to be independent of $(\omega_1 - \omega_3)$ which tells us that these terms can be relegated to nonresonant status.

For our experiment, we can rewrite (2.10) in a more abbreviated form. Since our chief interest is in scanning ω_1 through state $|b\rangle$, ω_2 and ω_3 are constant and ω_4 is approximately constant relative to any resonances for small change in ω_1 . Therefore

$$\chi_{\mu\alpha\beta\gamma}^{(3)}(\omega_4) \propto \frac{A_{\mu\alpha\beta\gamma}}{(\omega_{ba} - \omega_1 - i\Gamma_{ba})(\omega_{ca} - (\omega_1 + \omega_2) - i\Gamma_{ca})} + \chi_{NR}^{(3)} \quad (2.13)$$

where A is a constant containing the electric dipole matrix elements and factored sums of (2.10).

At this point, mention should be made of local field effects. \vec{E} used in the Hamiltonian of (2.3) is the

microscopic field $\vec{E}_{\text{loc}}(\vec{r}, t)$. This is equal to the microscopic field felt by the ion minus the field of the ion itself. It includes the light field plus all contributions from the charges in the medium and is highly sensitive to changes in position of neighboring ions. The macroscopic source polarization \vec{P} used in Maxwell's equations is defined using the macroscopic field $\vec{E}(\vec{r}, t)$. In order to amend the situation, a correction factor⁴⁰ is inserted in the polarization which contains polynomials of $\epsilon(\omega)$, where ϵ is the dielectric tensor. This could be a significant effect in certain cases in which additional resonant behavior could manifest itself. The tensor nature of ϵ also complicates things.

As discussed in Chapter 4, the spectral line narrowing is found to be dependent on parameters other than resonant behavior in the local field correction factor. Furthermore, all input beams are kept within small angles of the surface normal to the crystal. For uniaxial crystals with high symmetry, such as those used in our experiments, these small angles are unimportant so we shall ignore the correction factor in subsequent discussion.

Now that we know how the medium responds to the field \vec{E} through $\chi^{(3)}$, we are in a position to calculate the equation of propagation of the light through the crystal. The approach taken is generalized from Yariv.⁴¹ We start with the following experimental situation.

We have an absorbing crystal in which we are propagating three laser beams of different frequencies, all approximately along the \hat{x} direction and intersecting at small angles just inside the crystal surface. We assume traveling plane waves for the light fields and write for the total electric field in the interaction region inside the crystal

$$E_i(x, t) = \sum_{n=1}^4 E_i^n(x, t) \quad (2.14)$$

where

$$E_i^n(x, t) = \frac{1}{2} [E_{ni}(x) e^{i(\omega_n t - \vec{k}_n \cdot \vec{x})} + \text{c.c.}] \quad (2.15)$$

Four fields in (2.14) have been included to allow for the nonlinear generation of light at our signal frequency ω_4 . The subscript i gives the polarization, \hat{z} or \hat{y} .

These fields generate a polarization in the medium which acts as a source term in Maxwell's wave equation.

$$\frac{\partial^2}{\partial x^2} \vec{E} = \mu_0 \sigma \frac{\partial \vec{E}}{\partial t} + \mu_0 \epsilon_0 \frac{\partial^2 \vec{E}}{\partial t^2} + \mu_0 \frac{\partial^2}{\partial t^2} \vec{P}. \quad (2.16)$$

The polarization \vec{P} can be written as the sum of a linear and nonlinear part such that

$$\vec{P} = \epsilon_0 \chi_1 \vec{E} + \vec{P}_{NL} \quad (2.17)$$

where χ_1 is the linear electric susceptibility and, using the Einstein summation convention,

$$(\vec{P}_{NL})_i = \chi_{ijk}^{(2)} E_j E_k + \chi_{ijkl}^{(3)} E_j E_k E_l + \dots \quad (2.18)$$

We are interested in only those Fourier components of \vec{P} that drive the wave equation at $\omega_4 = \omega_1 + \omega_2 - \omega_3$, the frequency at which our signal occurs. Inserting $\vec{P}_{NL}(\omega_4)$ into (2.16) we find the field amplitudes (2.15) obey

$$\frac{dE_{1j}}{dx} = \frac{-\sigma_1}{2} \sqrt{\frac{\mu_0}{\epsilon_1}} E_{1j} - \frac{3i\omega_1^2}{4} \mu_0 \chi_{jkl}^{(3)} E_{2k}^* E_{3l} E_{4i} \exp[-i(\Delta\vec{k})_1 \cdot \vec{x}]/k_1$$

$$\frac{dE_{2k}}{dx} = \frac{-\sigma_2}{2} \sqrt{\frac{\mu_0}{\epsilon_2}} E_{2k} - \frac{3i\omega_2^2}{4} \mu_0 \chi_{klij}^{(3)} E_{3l} E_{4i} E_{1j} \exp[-i(\Delta\vec{k})_2 \cdot \vec{x}]/k_2$$

$$\frac{dE_{3l}}{dx} = \frac{-\sigma_3}{2} \sqrt{\frac{\mu_0}{\epsilon_3}} E_{3l} - \frac{3i\omega_3^2}{4} \mu_0 \chi_{lij}^{(3)} E_{4i}^* E_{lj} E_{2k} \exp[-i(\Delta\vec{k})_3 \cdot \vec{x}]/k_3$$

$$\frac{dE_{4i}}{dx} = \frac{-\sigma_4}{2} \sqrt{\frac{\mu_0}{\epsilon_4}} E_{4i} - \frac{3}{4} i \omega_4^2 \mu_0 \chi_{ijkl}^{(3)} E_{1j} E_{2k} E_{3l}^* \exp[-i(\Delta\vec{k})_4 \cdot \vec{x}] / k_4 \quad (2.19)$$

where $(\Delta\vec{k})_1 \equiv (\vec{k}_3 + \vec{k}_4 - \vec{k}_2 - \vec{k}_1) = (\Delta\vec{k})_2 = -(\Delta\vec{k})_3 = -(\Delta\vec{k})_4$

and where the slowly varying amplitude approximation

$$\left(\frac{\partial E_{ni}}{\partial x} \right)_{k_n} \gg \frac{\partial^2 E_{ni}}{\partial x^2} \quad \text{has been used. Subscripts } n \text{ on } \sigma_1, \epsilon_n,$$

k_n and E_{ni} indicate frequency dependence ω_n .

Equations (2.19) can be uncoupled if we allow beam depletion due to absorption, but not conversion to E_{4i} .

Thus we have immediately

$$\begin{aligned} E_{1j} &= E_{1j}(0) e^{-\alpha_1 x/2} \\ E_{2k} &= E_{2k}(0) e^{-\alpha_2 x/2} \\ E_{3l} &= E_{3l}(0) e^{-\alpha_3 x/2} \end{aligned} \quad (2.20)$$

where $\alpha_i = \sigma_i \sqrt{\frac{\mu_0}{\epsilon_i}}$ is the absorption coefficient at frequency ω_i . Setting $\Delta k_4 = \Delta k$ and using (2.20), the last of equations (2.19) can be readily integrated to give

$$E_{4i}(\mathbf{x}) = \frac{3}{4} \omega \sqrt{\frac{\mu_0}{\epsilon_4}} \chi_{ijkl}^{(3)} E_{ij}(0) E_{2k}(0) E_{3l}^*(0) (1 - e^{-i\Delta\mathbf{K}\cdot\mathbf{x}}) \times \exp(-\alpha_4 \mathbf{x}/2) / \Delta K \quad (2.21)$$

where $\Delta\vec{K} \equiv \Delta\vec{k} - i \Delta\vec{\alpha} / 2$

$$\text{and } \Delta\vec{\alpha} = (\alpha_1 + \alpha_2 + \alpha_3 - \alpha_4) \hat{\mathbf{x}} \quad (2.22)$$

The detected intensity at ω_4 is $\frac{1}{2}(\epsilon_4/\mu_0)^{1/2} |E_{4i}|^2$ so for an interaction length L the intensity is

$$I_{4i} = (L/2)^2 \exp(-\alpha_4 L) |\chi_{ijkl}^{(3)}(\omega_4) E_{1j}(0) E_{2k}(0) E_{3l}^*(0)|^2 \times G(\Delta K) \quad (2.23)$$

where $G(\Delta K)$, the phase matching factor, is given by

$$G(\Delta K) = \frac{1 + \exp(-\Delta\alpha L) - 2\exp[-\Delta\alpha L/2] \cos(\Delta k L)}{(\Delta k^2 + \Delta\alpha^2/4) (\frac{L}{2})^2} \quad (2.24)$$

For samples with inhomogeneously broadened transitions, $\chi^{(3)}$, $\Delta\alpha$, and $n(\omega)$ must be integrated over the entire linewidth. Inhomogeneous broadening will be discussed at the end of the chapter.

Equations (2.13), (2.23), and (2.24) constitute the main results of this section. (See Table 2.1.) They describe the two major effects of interest: resonant behavior and phase matching.

The phase matching factor $G(\Delta K)$ is present because

Table 2.1

Summary of Relevant Equations

$$\chi_{ijk\ell}^{(3)}(\omega_4) \propto \frac{A_{ijk\ell}}{(\omega_{ba} - \omega_1 - i\Gamma_{ba})(\omega_{ca} - (\omega_1 + \omega_2) - i\Gamma_{ca})} + \chi_{NR}^{(3)} \quad (2.13)$$

$$\text{where } \omega_4 = \omega_1 + \omega_2 - \omega_2.$$

$$\vec{\Delta K} = (\vec{k}_1 + \vec{k}_2 - \vec{k}_3) - \vec{k}_4 \text{ where } k_i = \omega_i n_i / c \quad (2.19)$$

$$\Delta\alpha = \alpha_1 + \alpha_2 + \alpha_3 - \alpha_4 \quad (2.22)$$

$$I_{4i} \propto (L/2)^2 \exp(-\alpha L) |\chi_{ijk\ell}^{(3)}(\omega_4) E_{1j}(0) E_{2k}(0) E_{3\ell}^*(0)|^2 G(\Delta K) \quad (2.23)$$

$$G(\Delta K) = (1 + \exp(-\Delta\alpha L) - 2 \exp(-\Delta\alpha L/2) \cos(\Delta k L)) / \left[(\Delta k^2 + (\Delta\alpha/2)^2) (L/2)^2 \right] \quad (2.24)$$

of the coherence of the nonlinear process. High efficiency is maintained only as long as the generated wave (or signal) at ω_4 remains in phase with the driving (or source) polarization throughout the region of interaction. The dispersive character of condensed media precludes phase matching for collinear beams where signal and source waves travel with different phase velocities in the medium. However, by crossing the beams inside the crystal at angles that satisfy $\Delta\vec{k} = 0$, phase matching is achieved and $G(\Delta K)$ is maximized.

A familiar form for $G(\Delta K)$ occurs in the totally nonresonant case ($\alpha_1 = \alpha_2 = \alpha_3 = \alpha_4 = 0$). Then $G(\Delta K)$ reduces to

$$G(\Delta k) = \frac{\sin^2(\Delta k L/2)}{(\Delta k L/2)^2} \equiv \text{sinc}^2(\Delta k L/2).$$

A graph of $\text{sinc}^2(\Delta k L/2)$ appears in Figure 2.2.

Figure 2.3 shows two-beam and three-beam phase matching diagrams. $\Delta\vec{k}$ is the degree to which the figures are unclosed and has a magnitude given by

$$\Delta k_1 = k_3 - (4k_1^2 + k_2^2 - 4k_1k_2 \cos \theta)^{\frac{1}{2}} \quad (2.25)$$

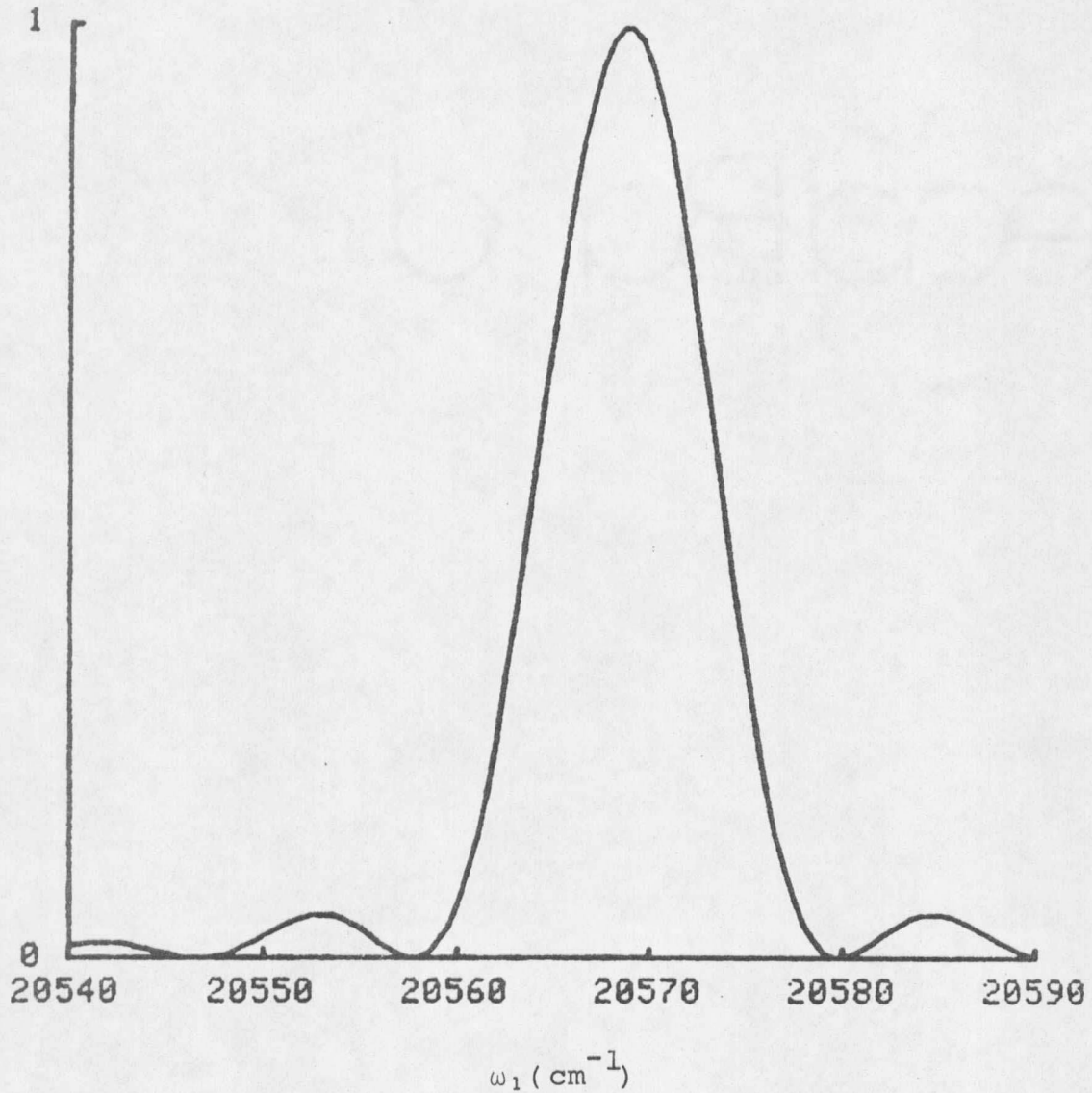


Figure 2.2. $\text{Sinc}^2(\Delta k L/2)$ vs. ω_1 using parameters in $\Delta k L$ relevant to the experiment. These include $L = 0.03$ cm, $n_1 = 1.508$, $\theta = 2.15^\circ$ and $k_2 = 1.646 \times 10^5 \text{cm}^{-1}$.

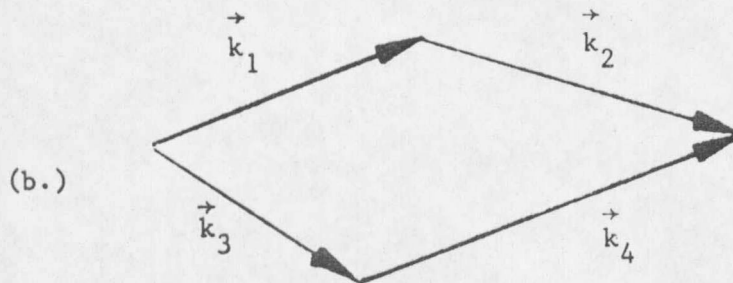
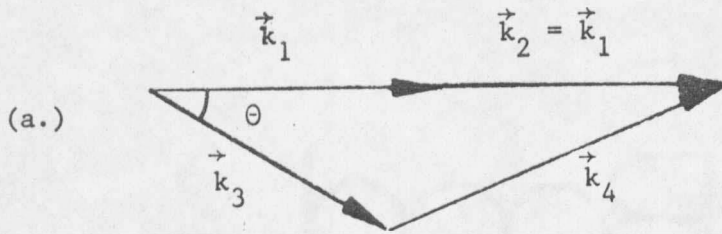


Figure 2.3. Phase matching diagrams showing (a.) 2- beam geometry with beam crossing angle θ , and (b.) the more general 3- beam geometry.

where $k_i = \omega_i n_i / c$. (2.26)

Note that the ω_4 beam (of wavevector \vec{k}_4) is directionally distinct from all other beams allowing for easy discrimination of the signal.

Besides phase matching, a second consequence of the nonlinear interaction is the possibility of interference between the nonresonant background signal and the real part of the susceptibility. This arises from

$|\chi^{(3)}|^2 = |\chi_{\text{res}}^{(3)} + \chi_{\text{NR}}^{(3)}|^2$ in (2.23). In most situations, $\chi_{\text{NR}}^{(3)}$ is approximately real while $\chi_{\text{res}}^{(3)}$ is complex. This gives

$$|\chi^{(3)}|^2 = (\chi_{\text{NR}}^{(3)\prime} + \chi_{\text{res}}^{(3)\prime})^2 + \chi_{\text{res}}^{(3)\prime\prime 2}$$

where the prime and double prime refer to real and imaginary parts of $\chi_{\text{res}}^{(3)}$ respectively. For significant values of $\chi_{\text{NR}}^{(3)\prime}$, the cross term can give a distinctly anomalous shape to the resonance.^{18,42} Therefore, in experiments where lineshape is important, interference must be considered.

Note that the above discussion has completely ignored any consideration of $\chi^{(2)}$. This is justified in centrosymmetric crystals where all even order terms in the \vec{P} expansion vanish due to symmetry considerations. This is not true for noncentrosymmetric systems (our case) and one

may ask whether $\chi^{(2)}$ contributes to the ω_4 signal.

Because the second order term involves only mixing of two light fields, no Fourier components directly appear at ω_4 . Such components can arise, however, in a two-step process.⁴³ First $\chi^{(2)}$ generates light at the frequencies $(\omega_1 + \omega_2)$, $(\omega_1 - \omega_3)$, and $(\omega_2 - \omega_3)$. The light at these frequencies can combine in the second step with the primary beams at $-\omega_3$, $+\omega_2$, and $+\omega_1$ respectively to achieve a signal at $\omega_4 = \omega_1 + \omega_2 - \omega_3$. We show in Chapter 4 that for the beam polarizations used in our experiment, $\chi_{izz}^{(2)} = 0$.

Finally, two assumptions need further elaboration. The first, used in deriving $\chi^{(3)}$ from ρ , involved the assumption of minimal population change from the initial conditions. In cases away from strong resonance, this is satisfactory. However, population dynamics ought to be considered in spectroscopy on strong transitions. We show in Appendix II that population changes are small for our case.

The second assumption was the plane-wave approximation made in solving Maxwell's wave equation. Laser beams are better described by Gaussian beam optics⁴⁴ in which the plane-wave approximation is valid only for areas inside the confocal region, b , of the beam focus. In this region, the beam wave fronts are planes; outside they begin to make

the transition to spherical waves. For $\frac{L}{b} \gg 1$, significant changes occur in phase matching and an approach such as that taken by Bjorklund⁴⁵ must be used. In our situation, however, $\frac{L}{b} \sim .02$ so that equation (2.23) is valid.

Materials

The active ion used in the experiments was terbium, which was hosted in concentrated form in $Tb(OH)_3$ and $LiTbF_4$. These compounds were chosen for purely pragmatic reasons; it was in $Tb(OH)_3$ that the narrowed FWM resonance was first observed. Initial interest in $Tb(OH)_3$ involved study of exciton dynamics associated with the $^5D_4 \mu = 2 - ^7F_5 \mu = 1$ transition.^{46,47} It was on the $^5D_4 \mu = 3^+$ state that the FWM signal was found. In retrospect the accessibility of energy levels, narrow linewidths, and transparency of the crystal makes these compounds extremely attractive for this kind of spectroscopy. The importance of each of these items will become clear in later chapters.

Several excellent reviews exist on rare earth spectroscopy.^{48,49} Much of this section is taken from Dieke⁵⁰ and Scott.⁵¹ A cursory description is given here in which only relevant highlights of energy levels and selection

rules are presented. A short section on spectral line broadening is presented at the end.

Rare earths are exceptionally attractive in solid state spectroscopy primarily because of their near atomic-like properties. These properties arise from the spatial contraction of the $4f^n$ radial wave-function known as the lanthanide contraction. For rare earth atoms which have large atomic number, the electronic shielding of the nucleus becomes less effective drawing the $4f$ electrons well inside the closed $6s$, $5p$, and $5s$ shells⁵⁰ encouraging very little participation with the environment. Chemical properties are very similar throughout the entire series--bond formation occurs first with the $6s$ electrons. Furthermore, the static electric field from other ions (known as the crystal field) by the $4f^n$ electrons is reduced to a small perturbation on the atomic Hamiltonian. Because interaction with the environment is limited, line-widths are correspondingly narrow.

The Hamiltonian for the rare earth ion in a crystalline host can be written as the sum of four terms each being a perturbation of the one preceding it. This is the material Hamiltonian given on page 12 and is equal

to

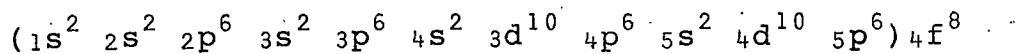
$$H_0 = H_1 + H_2 + H_3 + H_4 \quad (2.27)$$

where H_1 includes the kinetic term and central field potential of the nucleus, H_2 is the electrostatic potential between the electrons, H_3 is the spin orbit interaction, and H_4 is the static crystal field potential. The first three terms are associated with the free ion. The last arises from placing the ion in the host.

H_1 , in the central field approximation, can be written

$$H_1 = \sum_{i=1}^N \left(-\frac{\hbar^2}{2m} \nabla_i^2 + V(r_i) \right) \quad (2.28)$$

where $V(r_i)$ is the spherically symmetric potential each electron i sees from the nucleus. Equation (2.28) separates into N equations in electron coordinate r_i each satisfied by individual electronic wavefunctions having the good quantum numbers n, ℓ, s, m_ℓ, m_s . The energy depends only on n and ℓ giving rise to the configuration notation stating how many electrons have the same n and ℓ . The ground trivalent configuration of terbium is



where that part of the configuration in parenthesis represents all closed shells. To satisfy the Pauli exclusion principle, the eigenstates are Slater determinants of the individual electronic wave functions. All states within a configuration are degenerate.

The first two perturbations are given by

$$H_2 = \sum_{i>j} \frac{e^2}{r_{ij}} \quad (2.29)$$

where the sum is over all electron pairs, and

$$H_3 = \sum_{i=1}^N \zeta_i (\vec{l}_i \cdot \vec{s}_i) \quad (2.30)$$

They are approximately of the same magnitude so that neither Russell-Saunders nor j-j coupling methods work very well. An intermediate approach⁴⁹ is needed involving diagonalization of $\tilde{H} \equiv H_2 + H_3$. Typically, Russell-Saunders eigenfunctions (with good quantum numbers L and S) are first used as a basis set. This diagonalizes \tilde{H} in blocks of $J = L+S$ which is a good quantum number since the free ion retains full spherical symmetry. However, final diagonalization of each block yields wave functions that are linear

combinations of the Russell-Saunders terms so that, although final free ion levels are described by the notation $(2S+1)L_J$, it must be remembered that L and S are no longer good quantum numbers and the values listed are those of the greatest contributing term.⁵² Because the ground configuration is well isolated from the excited configurations inter-configuration interaction is small.

The final perturbation, H_4 , is from the static electric field of neighboring ions and it has the same site symmetry and strength for each ion in the crystal. Dynamic interactions with the lattice or ligands are ignored. When J-mixing is small, interactions are only allowed within the $2J+1$ components (termed the manifold of J) of each individual free ion energy level. Because the full rotational symmetry is now destroyed a certain amount of splitting is expected.

H_4 is expanded in a series of spherical harmonics⁵³

$$H_4 = \sum_{ikq} A_k^q r_i^k Y_k^q(\theta_i, \phi_i) \quad (2.31)$$

where $0 \leq k \leq \infty$ and $|q| \leq k$.

The basis which diagonalizes H_4 are the vectors $|\mu\rangle$ which are linear combinations of $|\alpha J m\rangle$ (α = those quantum numbers not listed). Depending on the site symmetry of the

ion, only those terms with certain values of q contribute to H_4 . This puts a restriction on the allowed values of m used in the $|\alpha J m\rangle$ expansion for $|\mu\rangle$. For the C_{3h} site symmetry of $Tb(OH)_3$, μ (called the crystal quantum number) takes on the values $\mu = 0, \pm 1, \pm 2, 3$. A second labeling convention is to use the label of the irreducible representation to which the state belongs. Figure (1a) shows the energy levels for $Tb(OH)_3$ and $LiTbF_4$ relevant to our experiments.

Once identification is made of how these states transform, group theoretical methods enable the selection rules for transitions to be worked out. Tables 2.2 and 2.3 give the selection rules for electric and magnetic dipole transitions for $Tb(OH)_3$ and $LiTbF_4$.

Note that pure f-f transitions are forbidden by electric dipole selection rules. However, odd parity components in the crystal field cause small amounts of configuration mixing which allow electric dipole transitions to take place. Judd-Ofelt theory⁵⁵ predicts transition intensities by using an effective transition operator formed from a tensor product of the electric dipole operator and odd parity components of the crystal field. In this model,

Selection RulesTable 2.2 -- Tb(OH)₃ allowed transitions⁵¹

μ	0	3	-2	2	1	-1
0	m σ	e π	e σ^+	e σ^-	m π^+	m π^-
3	e π	m σ	m π^+	m π^-	e σ^+	e σ^-
-2	e σ^-	m π^-	m σ	e σ^+	e π	m π^+
2	e σ^+	m π^+	e σ^-	m σ	m π^-	e π
1	m π^-	e σ^-	e π	m π^+	m σ	e σ^+
-1	m π^+	e σ^+	m π^-	e π	e σ^-	m σ

Table 2.3 -- LiTbF₄ allowed transitions⁵⁴

Γ	1	2	3, 4
1	m σ	e π	e σ , m π
2	e π	m σ	e σ , m π
3, 4	e σ , m π	e σ , m π	e π , m σ

Notation: "e" refers to electric dipole transitions. "m" refers to magnetic dipole transitions. " π " refers to the electric polarization parallel to the crystalline c axis. " σ " refers to the electric polarization perpendicular to the c axis.

the effective operator acts only on states of definite parity giving nonzero intensities to intra-configurational transitions.

The parity-allowed electric dipole $4f^n$ to $4f^{n-1}5d$ transitions are quite strong in comparison with f-f transitions. Because of the extended radial wave function of the $4f^7 5d$ level, ion-host interaction becomes much larger. Thus the influence of the crystal field is greater and interpretation of the spectra of those highly excited states becomes less straightforward.

Spectral Line Broadening

As mentioned earlier, a desirable feature of rare earth doped crystals is the narrow linewidths of the resonances. Even so, spectral line broadening exists to some degree and its sources can be grouped into two categories: inhomogeneous and homogeneous broadening.

Inhomogeneous broadening in solids arises from having slightly different crystal fields at each ion, causing a spread in the ensemble of energy levels for the crystal as a whole. This can come about through crystal strains, defects, and impurities. Its signature is usually a Gaussian lineshape although non-Gaussian distributions also occur.

Homogeneous broadening, yielding Lorentzian line shapes, has four contributions⁵⁶: (a) elastic, phase-destroying collisions, (b) inelastic collisions, (c) transitions to other levels for reasons other than (b), and (d) power broadening.

Elementary crystal excitations such as phonons and, in magnetic compounds, magnons are sources of elastic phase destroying collisions. An additional mechanism involves excitons in which the energy from the excited state of one ion is transferred to the unexcited state of a neighboring ion.⁵⁷ This occurs in $\text{Tb}(\text{OH})_3$ ^{46,47} in the form of Frenkel excitons where the excitation is coherent and possesses a well-defined wavevector.

Phonons, magnons, and excitons can also cause inelastic collisions. Not only does this contribute to population relaxation but loss of phase coherence as well. Exciton-exciton annihilation, recently discovered in $\text{Tb}(\text{OH})_3$ and LiTbF_4 ⁵⁸, occurs upon application of intense laser fields.

Transition to other levels for reasons other than inelastic collisions can be due to a number of causes. Spontaneous emission gives rise to the natural line width. Other cooperative processes include near resonant or intra-

line energy transfer and nonresonant or interline transfer.⁵⁹ Both cases involve phonon-assisted multipolar or exchange interactions. The intraline case occurs within a strain broadened line while the interline case occurs between different ions with energy levels differing by amounts greater than kT and/or the inhomogeneous linewidth.

In certain systems where it is favored by the energy level scheme, two-step absorption can occur. Although we were not able to conclusively measure this process in our Tb compounds,⁶⁰ it might be competing with the observed exciton annihilation processes.

Power broadening arises from stimulated emission. An exact solution of (2.4) can be derived for a two level system⁶¹ giving a power dependent linewidth to the Lorentzian shape. For small fields it reduces to the natural line shape.

Homogeneous linewidths can be directly related to the decay constants Γ_{nn} of (2.5). In the absence of power broadening

$$\Gamma_{nn} = \left(\frac{\Delta\nu_{nn}}{2} \right)$$

where $\Delta\nu_{nn'}$ is the full width at half the maximum value of the line (FWHM). The dephasing time, or time it takes the induced dipole moment to lose its coherence due to all the above mechanisms except power broadening, is

$$(T_2)_{nn'} = (2H\Gamma_{nn'})^{-1}$$

Direct measurement of T_2 using a coherent transient form of FWM is described in Appendix I.

In general, both homogeneous and inhomogeneous broadening are present in line spectra; sometimes one dominates the other. Variation of different experimental parameters controls the broadening mechanisms. At low temperatures phonons "freeze out" relieving the system of such a major contribution to homogeneous broadening that inhomogeneous strain broadening plays the major role. Likewise, magnons, freeze out in applied magnetic fields. Exciton density is a function of laser power. At room temperature, phonon broadening dominates to the point where it masks information about the other, less understood, dephasing mechanisms. Thus, for our experiments, cooling with liquid helium was used, freezing out phonons leaving us with inhomogeneously broadened lines.

Chapter 3

APPARATUS AND SAMPLES

The spectroscopic system used was designed to be as universal as possible in performing optical experiments. The lasers and associated optics were mounted on optical breadboards or benches facilitating easy placement and changeability of components. Experiments requiring a magnetic field used a homemade stainless steel dewar with a superconducting solenoid while other experiments used a smaller moveable glass Dewar. The electronics had both continuous and pulsed signal capability.

The description of the apparatus which follows is divided into sections that describe the system optics, lasers, Dewars, and electronics. A short section on the samples is presented at the end.

System Optics

This section deals with the generation, manipulation, and propagation of the laser beams into the sample as well as the efficient collection of the light emitted from the sample. Figure 3.1 shows a schematic diagram of the entire spectroscopic system. The lasers can be operated individually or together and the beams directed into either Dewar (to be discussed later). The glass Dewar is easily

removable to allow collection of light from the metal Dewar by the Spex monochromator.

An important consideration in four-wave mixing experiments is to ensure that the waists (or foci) of all three input beams are of similar size and located at the input side of the crystal. Because of the differences in the positions of each of the dye lasers, this required a total of five lenses: three separate lenses at the output of each laser to give a similar conjugate waist for each beam, and two more lenses common to all three beams to define the final waist size and position at the proper place. Figure 3.1 shows values for the lenses for a typical three-beam experiment in the glass Dewar. The chosen lenses gave waists (one-half of the beam diameter) of 30-40 microns.

It should be noted that rough values for the focal lengths and positions of the lenses could be chosen on the basis of ray optics calculations in most, but not all cases. The cross-sectional profile of the dye laser beams is closely approximated by a Gaussian function; hence Gaussian beam optics⁴⁴ are more appropriate than ray optics. It is not hard to show that for $(\frac{\pi \omega_0^2}{\lambda})^2 \ll (L-f)^2$ Gaussian beam optics reduce to ray optics and the simpler ray formulas

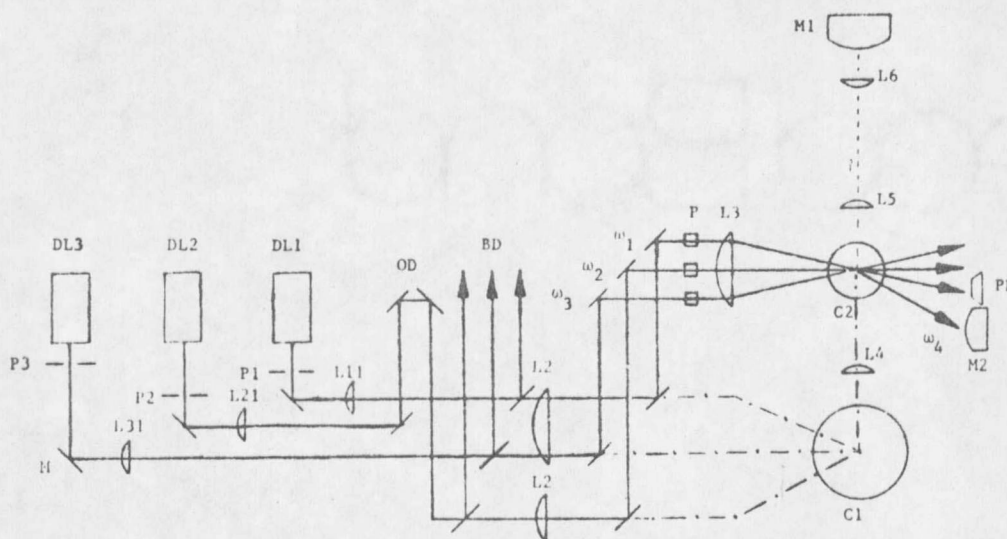


Figure 3.1. Optical system used in FWM experiments. Components are the following: DL1,2,3 -dye lasers at frequencies $\omega_1, \omega_2, \omega_3$, respectively;

OD - 79 cm optical delay
 P - polarizing prisms
 PD - photo diode detecting
 ω_1 beam absorption
 M2 - MacPherson monochromator detecting ω_4 signal.

P1,2,3 -pin holes;
 M - mirror or 90° prisms
 M1 - Spex monochromator for fluorescence collection
 C1, C2 - stainless steel Dewar, glass Dewar

Beam Optics

Lens	Focal Length	Position cm
L1.1	36 cm	DL1-L1.1:42.5
L2.1	57 cm	DL2-L2.1:58.4
L3.1	40 cm	DL3-L3.1:49.5
L2	-67 cm	DL1-L2: 95.5
L3	25 cm	L3-C2 (axis):30.5

Collection Optics

Lens	Focal Length	Position cm
L4	33.3 cm	L4-C1 (axis): 11.4
L5	5.1cm f/ 1.5	L5-C2 (axis): 6.0
L6	5.1cm	L6-M1 (slit): 5.0

Other Distances

DL1-P1:18.4 cm
 DL2-P2:22.2 cm
 DL3-P3:14.6 cm

may be used (ω_0 = beam waist inside laser cavity, λ = wavelength, L = distance from the waist position to the lens, and f = focal length of the lens). In most situations, this was the case. However, in certain instances, notably in the index experiment discussed in Appendix II, Gaussian beam calculations were necessary.

An optical wedge was used to split off part of the beam for laser diagnostic purposes. This enabled frequency stability, pulse energy, and in the case of the mixing experiments, the relative timing of the pulses to be observed without introducing spurious Fabry-Perot behavior.⁶² Fabry-Perot effects were an ever present problem and were dealt with by tilting surfaces so as to eliminate internal reflective interference or by avoiding the use of parallel optical surfaces altogether.

Absorption data were taken in either of two ways: using a tungsten-halogen lamp and scanning the monochromator, or scanning a narrow-band dye laser with a spectrally insensitive detector such as a photodiode or the monochromator with wide slits.

The optics for the laser absorption were as depicted in Figure 3.1. The ω_1 beam absorption was monitored at the exit window of the dewar simultaneously with

the four-wave mixing signal allowing exact spectral synchronization of the signal with the absorption. This both avoided problems related to laser drift and speeded up the accumulation of data.

The monochromators used included a Spex Model #14018 0.85-meter Czerny-Turner Double Monochromator with two 1800 groove/mm holographic gratings and a McPherson Model #218 0.3 meter monochromator with a 1200 l/mm grating blazed at 5000 Å.

Fluorescence collection was achieved by observing the side profile of the laser beam going through the crystal. In some cases, this was adequate. However, in highly absorbing crystals such as the ones in these experiments, distorted line shapes occurred. In such situations a back scattered collection geometry is better. More will be said about this later.

Lasers

Two homemade nitrogen lasers generating 10 nsec pulses pumped up to three tunable dye lasers. One, a single beam model, pumped the ω_1 laser with a peak power of 550 kW. The other, a double-beam model, pumped the ω_2 and ω_3 lasers with a total (double-beam) power of 580 kW.

The three dye lasers were of the Hänsch type⁶³

with one of them (ω_1 laser) operating in the high resolution, etalon-narrowed, oscillator-amplifier mode to give a 45 kW beam with $0.03-0.05\text{cm}^{-1}$ linewidth. This was the laser that was scanned through the $^5\text{D}_4$ transition. Dye laser pulses lasted 5 nsec.

Dewars and Dewar Optics

Two separate dewars were used throughout the experiments. The metal one housed a 60 kG superconducting solenoid built by American Magnetics, and was used for initial survey experiments with and without magnetic fields. The glass dewar, purchased from Pope Scientific, was used during the later stages of data taking.

Because of the difficulty in determining the waist positions of the beams relative to the sample inside the dewar, a pair of orthogonal razor blades placed on an X-Y translation mount was located at a conjugate sample position outside the dewar. Sending the beams to the blades via a removable mirror enabled not only the waists to be put in their proper position but also allowed adjustments to be made to ensure the beams were crossed at the waist position.

Electronics

An important consideration of the mixing experi-

ments involved firing the lasers at the same time or, in other cases, providing for a variable delay between the firing of the ω_1 laser and the firing of the ω_2 and ω_3 lasers. To gain this capability, Douglas Jones designed the electronic trigger and delay unit used to trigger the two nitrogen lasers. Pulse jitter was less than one nanosecond. Laser repetition rates used were $3\frac{1}{3}$ pps during early experiments and 10 pps during the final ones.

The signals from the photomultiplier tubes collecting light from the monochromators were sent to either a Keithley 416 picoammeter or a Princeton Applied Research 162 boxcar averager (or both in the case of the synchronized absorption and mixing experiments). Data was then temporarily stored on a Northern Scientific 575 multi-channel analyzer, then transferred and stored on disks via a CRDS MF-211 computer (DEC LSI 11).

Samples

The experiments were carried out on several different samples of the compounds $\text{Tb}(\text{OH})_3$ and LiTbF_4 .

The $\text{Tb}(\text{OH})_3$ crystals, obtained from Professor Werner Wolf, were grown using a hydrothermal technique⁶⁴ developed by H. E. Meisner of Yale University. They grow in the form

of a hexagonal needle parallel to the c axis and are small, being on the order of 2 mm long and 250 to 350 μm thick. There are two ions per unit cell with C_{3h} point symmetry.^{65,66}

The LiTbF_4 crystals were cut from a boule obtained from H. J. Guggenheim of Bell Laboratories, Murray Hill. The sample used in the mixing experiment was oriented, cut, and polished by Mark Ritter in the shape of a rectangular prism of dimensions 0.55 x 1.04 x 3.61 mm. The long dimension is parallel to the c axis. LiTbF_4 has four ions per unit cell with S_4 point symmetry.^{67,68} The damage threshold was empirically measured to be 875 MW/cm^2 .

Chapter 4

RESULTS AND DISCUSSION

As discussed in Chapter 1, the initial observation of the FWM signal raised two major questions. The first dealt with the exact nature of the nonlinear process itself. The second involved explaining the narrowed lineshape and its location within the absorption profile. An additional complication arose upon the observation of a splitting in the fluorescence excitation of the ${}^7F_6 - {}^5D_4$ transition when none was observed in the absorption. See Figure 4.1. Determination of the relationship (if any) between the splitting and the FWM signal needed to be made

Because most of the experiments were done with two input beams of frequencies ω_1 and ω_3 rather than the more general case of three input beams, subsequent discussion will deal with the two beam case (we have $\omega_4 = 2\omega_1 - \omega_3$ for $\omega_2 = \omega_1$). Exceptions will be noted.

Nature of Signal

The ω_4 signal was detected upon application of two beams of frequencies ω_1 and ω_3 while ω_1 was scanned through the intermediate resonance $|b\rangle$ of Figure 2.1(a). Crystal temperature was 1.3 K. The fact that light mixing was

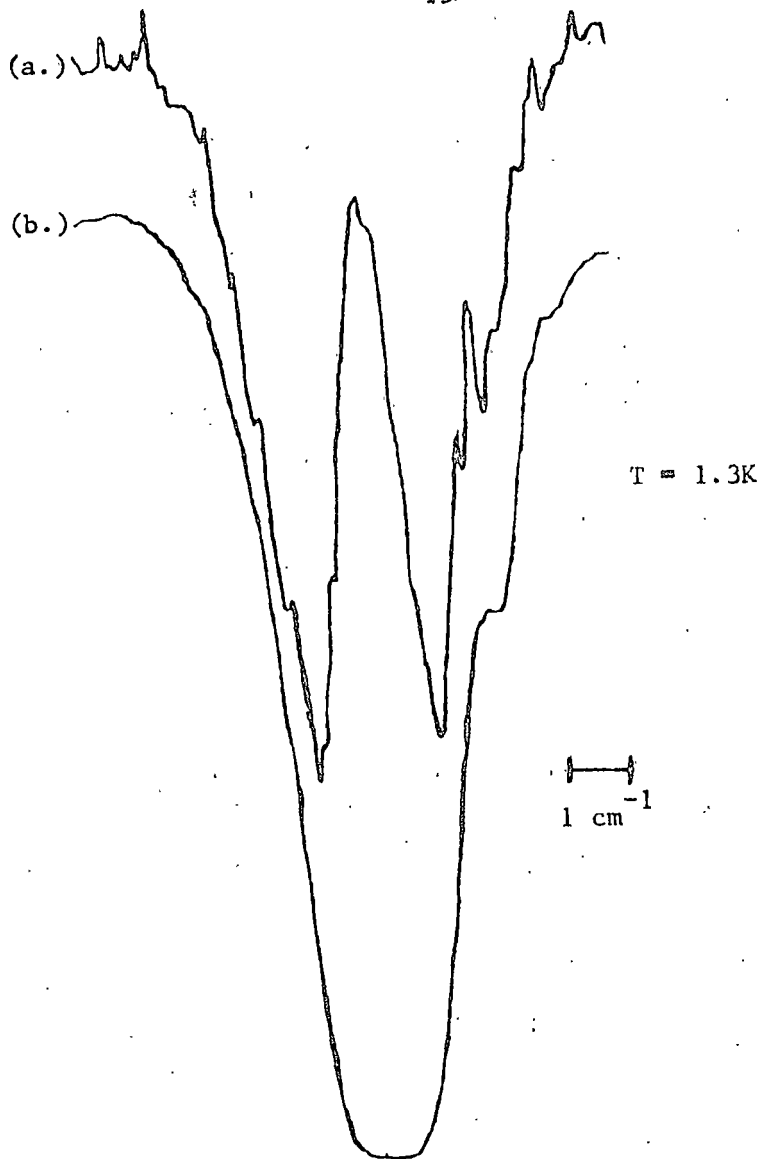


Figure 4.1. (a.) Fluorescent excitation spectrum showing splitting $5D_4 \mu=3^+$ state. $B = 50kG$. Splitting was also observed in $LiTbF_4$. Spectrum was taken by scanning ω_1 through resonance while monitoring the fluorescence intensity. (b.) Corresponding absorption.

occurring, the necessity for temporal and spatial overlap of pulses, and the directionally distinct ω_4 output all strongly suggested a third order nonlinear interaction such as CARS or TPAFWM.

Nevertheless, other processes could account for these observations. They include the two-step process involving $\chi^{(2)}$ or higher order processes⁶⁹ of $\chi^{(n)}$ for $n \geq 3$.

The higher order processes may be ruled out on the basis of the observed dependence of the signal intensity on the power of the input beams. From equation (2.9), the intensity dependence of ω_4 signal on the input beam intensities for any particular order can be determined. Thus, for a third order process, the sum of the powers of the input intensities is three. A fourth order process sums to four, etc. Figure 4.2 shows the power of the ω_4 signal as a function of the ω_1 beam power and ω_3 beam power respectively for the two-beam experiment. We find a quadratic dependence for the ω_1 power and a linear dependence for the ω_3 power. We thus have $n \leq 3$.

The two-step second order process can be eliminated as a possibility by symmetry considerations. For all experiments (unless otherwise noted), both input beams

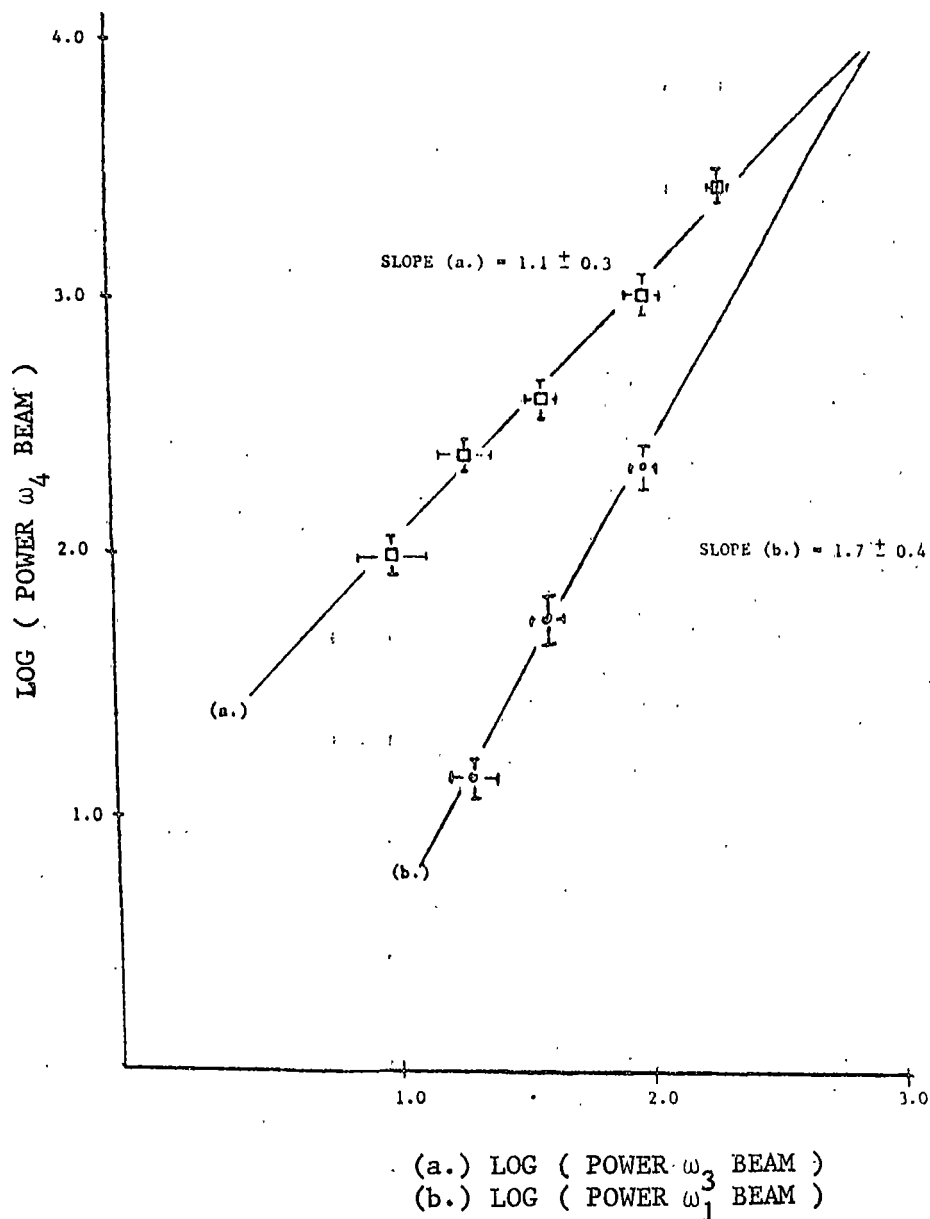


Figure 4.2. Log (signal power) as a function of log (input power) for (a.) ω_3 beam and, (b.) ω_1 beam, in 2-beam experiment in $Tb(OH)_3$.

and signal were Π polarized (\vec{E} parallel to c axis). $\chi_{izz}^{(2)}$ vanishes for both C_{3h} ($Tb(OH)_3$) and S_4 ($LiTbF_4$) point symmetries for all i .⁷⁰ Therefore, the second order process cannot occur, and we are left with only $\chi^{(3)}$ as the mixing mechanism.

A CARS signal can also be discounted as it would have a strong $(\omega_1 - \omega_3)$ dependence. Figure 2.1C shows the relevant energy level diagram. If CARS were involved, choosing different values for ω_3 would move $(\omega_1 - \omega_3)$ in and out of resonance with states in the 7F_J manifolds, thereby changing the signal strength. No such change was observed. As a further precaution, ω_1 and ω_3 were chosen to avoid any Raman resonances. These were obtained from spontaneous electronic and phonon Raman spectra measured previously and from Table 4.1, which lists the electronic energy levels of the 7F term. Unless otherwise noted, ω_3 was chosen to be 18301 cm^{-1} for $Tb(OH)_3$ and 17422 cm^{-1} for $LiTbF_4$.

The elimination of the above third order processes focused our attention on TPAFWM. Examination of selection rules showed that $\chi_{zzzz}^{(3)}$ is allowed under the C_{3h} and S_4 point symmetries of $Tb(OH)_3$ and $LiTbF_4$.⁷⁰ As seen from equation (2.10), electric dipole selection rules operate

Table 4.1

 7F_J Energy Levels(a) $Tb(OH)_3$ at 4.2K, ⁵¹ experimental values in cm^{-1}

<u>J</u>	<u>μ</u>	<u>Energy</u>	<u>J</u>	<u>μ</u>	<u>Energy</u>
6	0+	0.0	4	3+	-
	0-	0.0		2	3476.1
	1	118.2		3-	3473.1
	2	206.0		0	3483.4
	0+	224.4		1	3539.2
	1	233.7		2	3600.7
	3+	-			
	2	252.3			
	3-	-			
5	3-	2082.0	3	1	4428.6
	2	2143.9		3-	4478.8
	1	2170.9		2	4485.2
	3+	2229.1		0	4484.3
	2	-		3+	4540.5
	1	2323.9			
	0	-			

 ${}^7F_2 - {}^7F_0$ manifolds undetermined.

(b) LiTbF_4^{68} at 10K, theoretical values in cm^{-1}

<u>J</u>	<u>μ</u>	<u>Energy</u>	<u>J</u>	<u>μ</u>	<u>Energy</u>
6	2	0	4	1	3325
	2	2		2	3399
	3,4	108		3,4	3400
	1	119		1	3539
	2	135		2	3572
	3,4	175		3,4	3630
	1	223		1	3845
	1	376			
	3,4	390	3	2	4324
	2	401		3,4	4404
				1	4478
5	2	2087		3,4	4528
	3,4	2089		2	4536
	1	2130			
	1	2148	2	1	5024
	3,4	2162		2	5064
	1	2339		3,4	5285
	3,4	2390		2	5371
	2	2403			
			1	1	5603
				3,4	5714
			0	1	5923

in a step-wise fashion for the transitions associated with χ_{res} . Tables 2.2 and 2.3 show that electric dipole transitions are allowed between states $|a\rangle$ and $|b\rangle$ of Figure 2.1 (a) for the quantum numbers involved in our experiments. In order to determine if multiresonant enhancement was taking place, Paula Fisher took linear UV absorption scans on both $Tb(OH)_3$ and $LiTbF_4$. Her results are given in Figure 4.3. They indicate that $2\omega_1$ falls in the broad $4f^75d$ absorption band.⁷¹ Because the mixing process utilizes an intermediate $4f^8$ state, the strong parity allowed transition to the $4f^75d$ band provided major enhancement to the mixing.

To gain final confirmation of the two-photon resonant nature of the FWM spectra, a three-beam mixing experiment was performed in which ω_2 was tuned away from ω_1 . The results, shown in Figure 4.4 indicate (a) that signal enhancement of over twenty-five times is available by choosing $(\omega_1 + \omega_2)$ to fall on resonance in the three-beam experiment, and (b) the upper energy wing of the two-photon resonance is utilized in the two-beam experiment in which $\omega_2 = \omega_1$. We have thus identified the FWM as doubly-resonant, two-photon-absorption-induced FWM. The two-photon resonance has important applications to be discussed

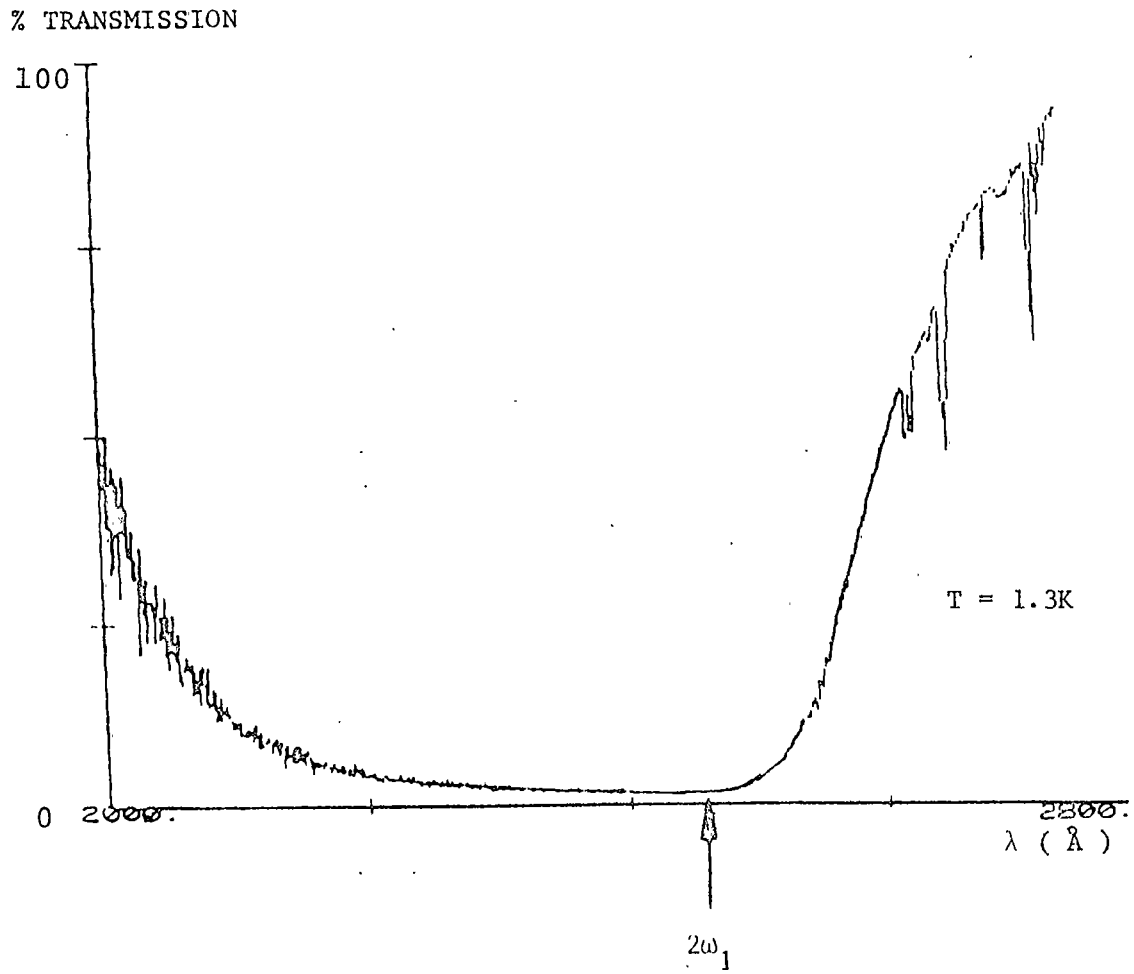


Figure 4.3. Broad linear UV absorption band in $\text{Tb}(\text{OH})_3$ associated with excited state in TPAFWM.

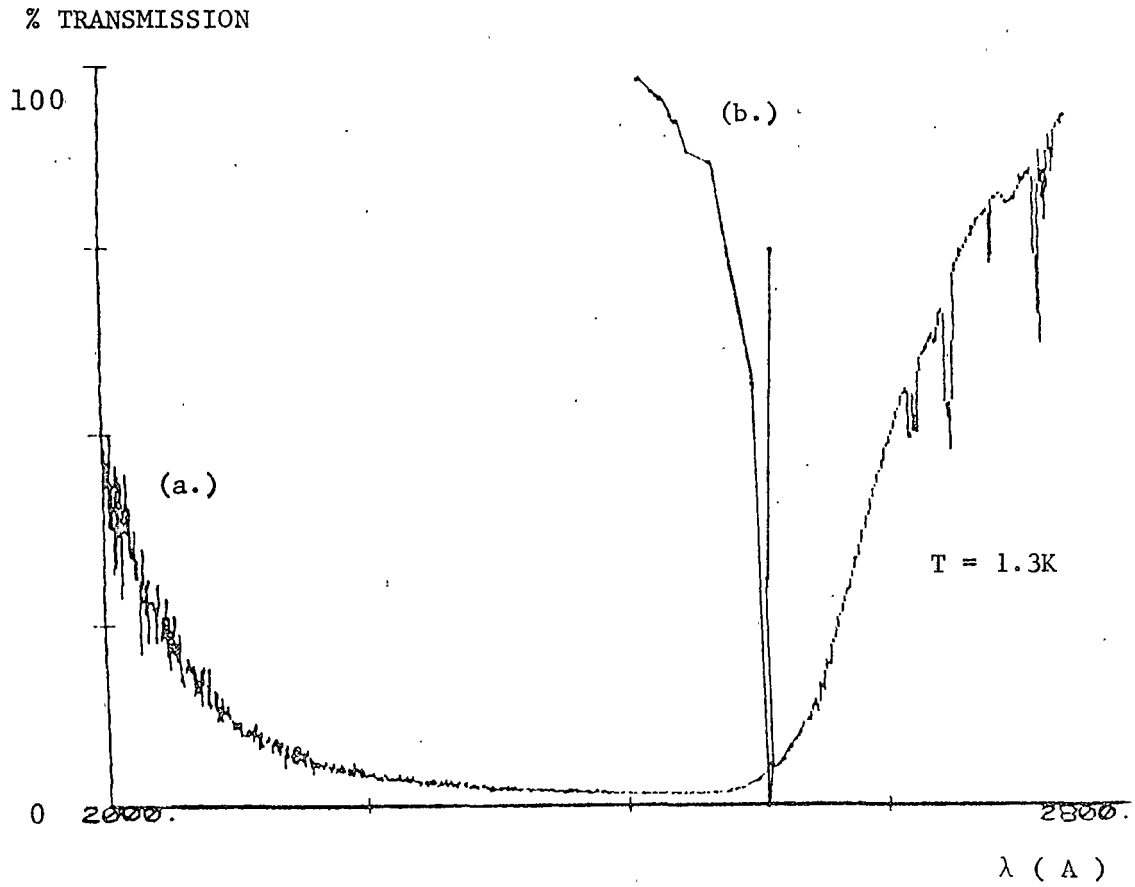


Figure 4.4. (a.) Broad $4f^7 5d$ absorption band, $Tb(OH)_3$, and (b.) resolved crystal field component using TPAFWM.

later.

Line Narrowing

Upon first observation of the line narrowing, we were faced with consideration of several possible explanations. To begin with, crystal defects could cause narrowing by giving rise to broken symmetries. This would enable different selection rules to operate in different parts of the inhomogeneous distribution, thus favoring one section over the other. If this were the case, sensitivity to samples obtained from different batches would be possibly exhibited. None was seen for $TB(OH)_3$.

Second, narrowed lines approximating homogeneous linewidths can be obtained under certain conditions using special resonances in the susceptibility.⁷³ However, such conditions are of limited generality and did not apply to our experiment.

Third, the FWM could be narrowed by using a selection rule favoring only one side of the splitting obtained in the fluorescent excitation spectrum of Figure 4.1. While this explanation was discounted by other observations, a splitting may play a role in explaining the finer details of our data. This will be discussed shortly.

Finally, it should be mentioned that interference effects between resonant and nonresonant contributions to the susceptibility may lead to dispersive-like lineshapes.⁴² Although this would not significantly narrow the lines, it could complicate the determination of the actual line narrowing mechanism. Fortunately, in our case, the non-resonant background was much less than the resonant signal thereby minimizing the interference.

In order to pin down the cause of the narrowing, all experimental parameters were systematically varied. It was found that the major variable affecting both the spectral position and shape of the ω_4 signal within the inhomogeneous absorption was the beam crossing angle inside the sample. See Figure 4.5.

None of the above explanations can account for this observed angle dependence. Instead, the following qualitative model has been developed, based upon the inclusion of the dispersive nature of the index of refraction on the phase matching conditions. In all other treatments of phase matching, anomalous index dispersion has been ignored.

From equation 2.26, we have $k_1 = \omega_1 n_1 / c$. We can treat $\alpha_3 = \alpha_4 \approx 0$ so that for all beams Π polarized in the two-beam experiment, equation (2.23) becomes

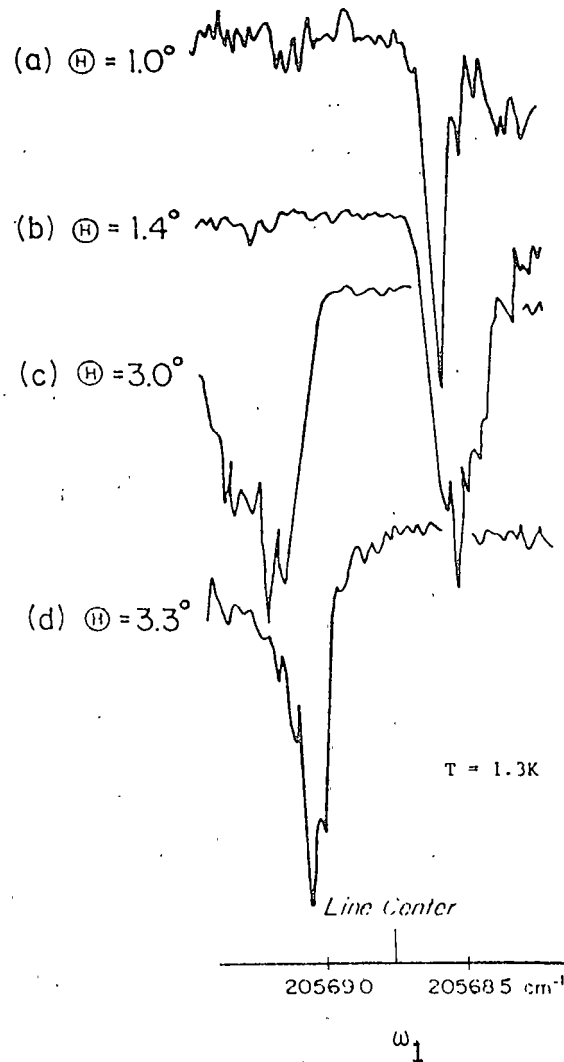


Figure 4.5. Four-wave mixing signal at ω_4 as a function of ω_1 for several internal beam crossing angles θ in LiTbF_4 . $\omega_3 = 17422\text{ cm}^{-1}$.

$$I_{4Z} \propto \left| \chi_{ZZZZ}^{(3)}(\omega_4) \right|^2 I_{1Z}(0) I_{3Z}(0) [1 + \exp(-2\alpha_1 L) - 2\exp(-\alpha_1 L) \cos(\Delta k L)] / (\Delta k^2 + \alpha_1^2) \quad (4.1)$$

where $\Delta \vec{k} = (2k_1 - k_3) - k_4$, the degree of phase mismatch. Scanning ω_1 through resonance changes Δk in two ways. It depends directly on ω_1 and can change indirectly through the dispersive nature of $n_1(\omega_1)$. For spectral lines with small widths, the first way is insignificant. The second way, however, becomes important when scanning through a resonance.

The intensity of the ω_4 signal drops off in those areas of the resonance where the dispersive change in the index rules out phase matching; a narrowed signal results. The position of the signal within the inhomogeneous line is determined by $n_1(\omega_1)$, while the width of the signal is governed by $dn_1/d\omega_1$. In situations where $dn_1/d\omega_1$ is steep enough, the narrowing is limited only by the homogeneous width of the transition.

Figure 4.5 shows the data obtained by monitoring the intensity of the ω_4 signal while the ω_1 beam was scanned through the 5D_4 state. Four different internal crossing angles are shown. Note that the signal is much narrower than the corresponding white-light absorption coefficient of

Figure 4.6 (a) which is expected to give a measure of the shape of the inhomogeneously broadened $\chi^{(3)}$.

As the internal crossing angle θ increases from 1.0° to 1.4° , the value of k_1 which satisfies the phase matching condition shrinks, and the signal moves to the low energy side of the transition. It also broadens consistent with moving toward a flatter part of the index dispersion curve. Increasing the angle from 1.4° to 3.0° drives the line to the high energy side of the absorption profile as phase matching occurs for smaller index. Finally, increasing θ to 3.3° pushes the signal more toward line center and narrows it corresponding to the steeper index region.

Additional observations have been made which reinforce the index model. By holding the crossing angle fixed and tuning ω_3 , results are obtained similar to those involving changes of angle. The narrowed line can again be driven from one side of the transition to the other as would be expected due to changes in phase matching (see Figure 4.7). In $\text{Tb}(\text{OH})_3$, for $\theta = 4.4^\circ$, narrow lines occur on the high energy side of the ${}^5\text{D}_4$ ω_1 resonance when $\omega_3 = 18301 \text{ cm}^{-1}$ and occur on the low energy side of the ω_1 resonance when $\omega_3 = 16900 \text{ cm}^{-1}$. Finally we note that a

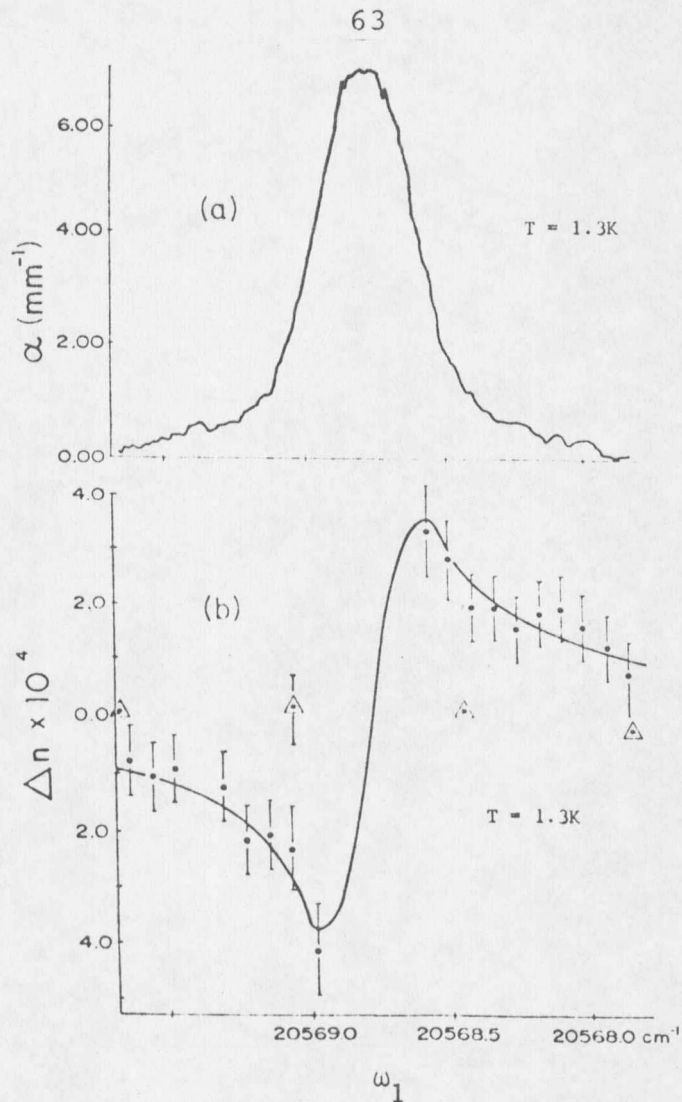


Figure 4.6. (a) White-light π polarized absorption coefficient for ${}^5\text{D}_4 \Gamma_1$ state of LiTbF_4 taken with 0.1 cm^{-1} resolution and (b.) index of refraction of the same state. Crystal data: dots; control data with crystal removed: dotted triangle. The single error bar on the control point is typical. The horizontal axis is the same for both graphs.

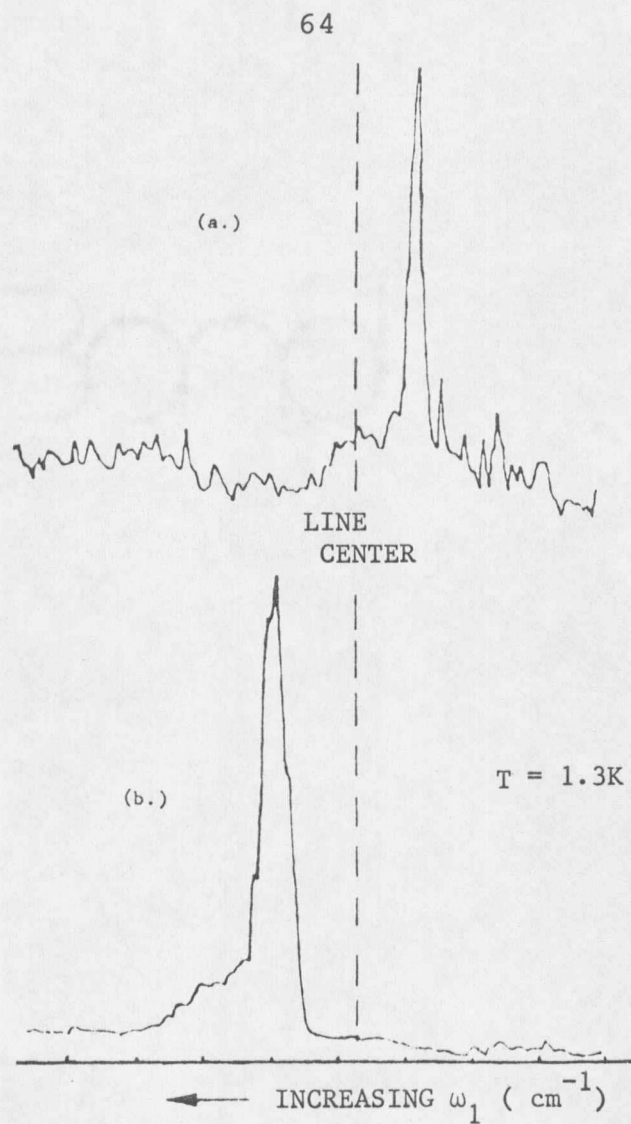


Figure 4.7. Dependence of FWM signal on ω_3 . Internal crossing angle fixed at $\theta = 4.4^\circ$. (a.) $\omega_3 = 16900$. (b.) $\omega_3 = 18301$. $\text{Tb}(\text{OH})_3$.

complete set of phase matching versus angle data has been obtained on the $^5D_4 \mu = 3^+$ state of $Tb(OH)_3$ (Figure 4.8) and that narrowed lines have been observed on other transitions in both compounds.

While good qualitative agreement is obtained from the index model, it must be realized that present day nonlinear optical theory is severely taxed to include a full description of all the interactions actually occurring. Intrinsic phenomena such as exciton behavior, pump depletion, inhomogeneous broadening, and higher order effects in the refractive index may all need to be considered. Experimental parameters such as finite laser band widths and power broadening might also be important.

In spite of all this, an attempt was made to quantitatively check the above model. Direct measurement of the linear index of refraction as ω_1 scanned through resonance was made. A description of the experiment is given in Appendix II. The results are shown in Figure 4.6 (b). The measurements of the index and white light absorption provided the necessary parameters to plot equation (4.1). For convenience, a Lorentzian lineshape for α was used. This avoided numerical integration (to be discussed shortly).

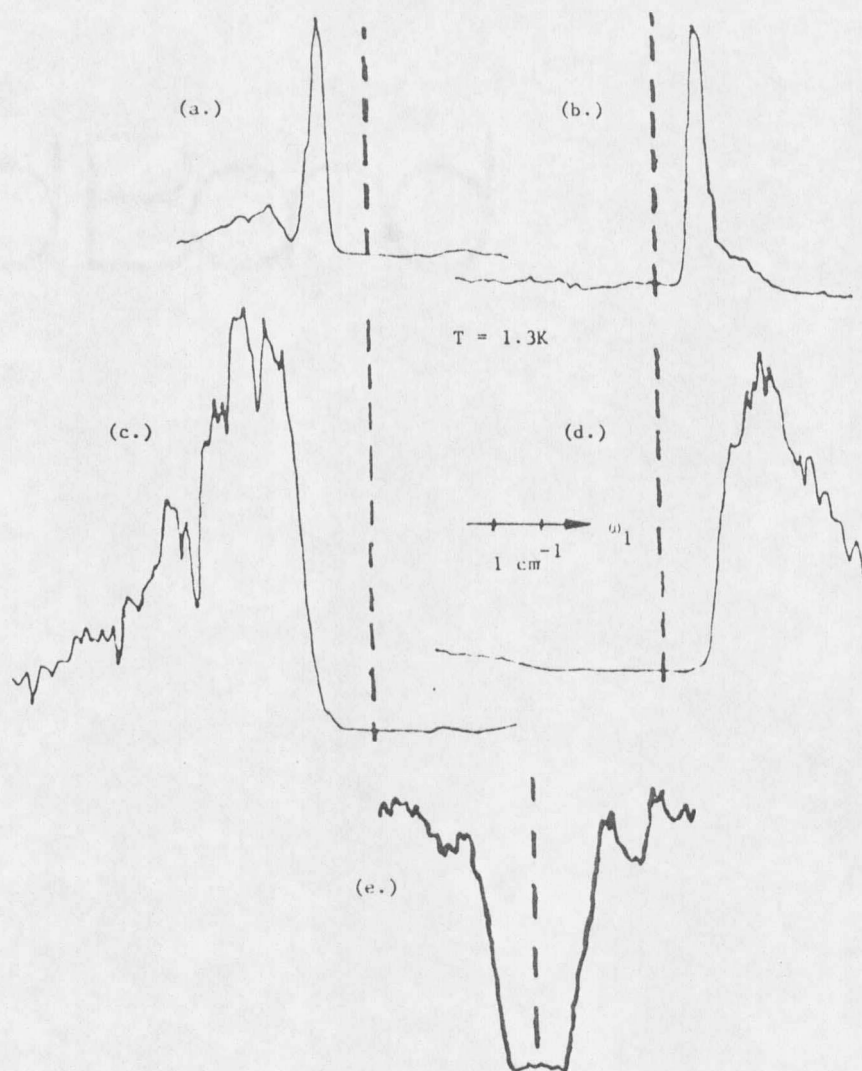


Figure 4.8. FWM signal at ω_4 for different internal angles θ in $\text{Tb}(\text{OH})_3$. Dashed lines refer to line center. $\omega_3 = 18301 \text{ cm}^{-1}$. (a.) $\theta = 1.6^\circ$, (b.) $\theta = 4.4^\circ$, (c.) $\theta = 2.5^\circ$, and (d.) $\theta = 3.5^\circ$. (e.) corresponding absorption.

The simulation, shown in Figure 4.9, indicates that the magnitude of Δn is only great enough to distinguish between the top and bottom of the dispersion curve, moving the signal from one side to the other upon change of angle but giving linewidths much too large.

In Figure 4.10 we increase the magnitude of Δn by a factor of 3.8. Here we get the correct spectral motion of the signal along with the appearance of a distinct central peak resulting from phase matching occurring on the inside portion of the dispersion curve. The signals are still wider than those measured.

Finally, Figure 4.11 shows the effect of greatly increasing n by 35 times. The spectral narrowing of the signal (on the outside part of resonance) is now equal to that of the narrowest line we have measured (approximately the laser linewidth). Assuming that the $n_1(\omega_1)$ measurements are accurate, this leads to the possibility that $\chi^{(3)}$ is adding to the linear index of refraction in the mixing experiments.

Note that the above model is highly sensitive to the magnitude and probably the shape of absorption and index profiles. Comparison of Figures 4.12 and 4.13 with Figure

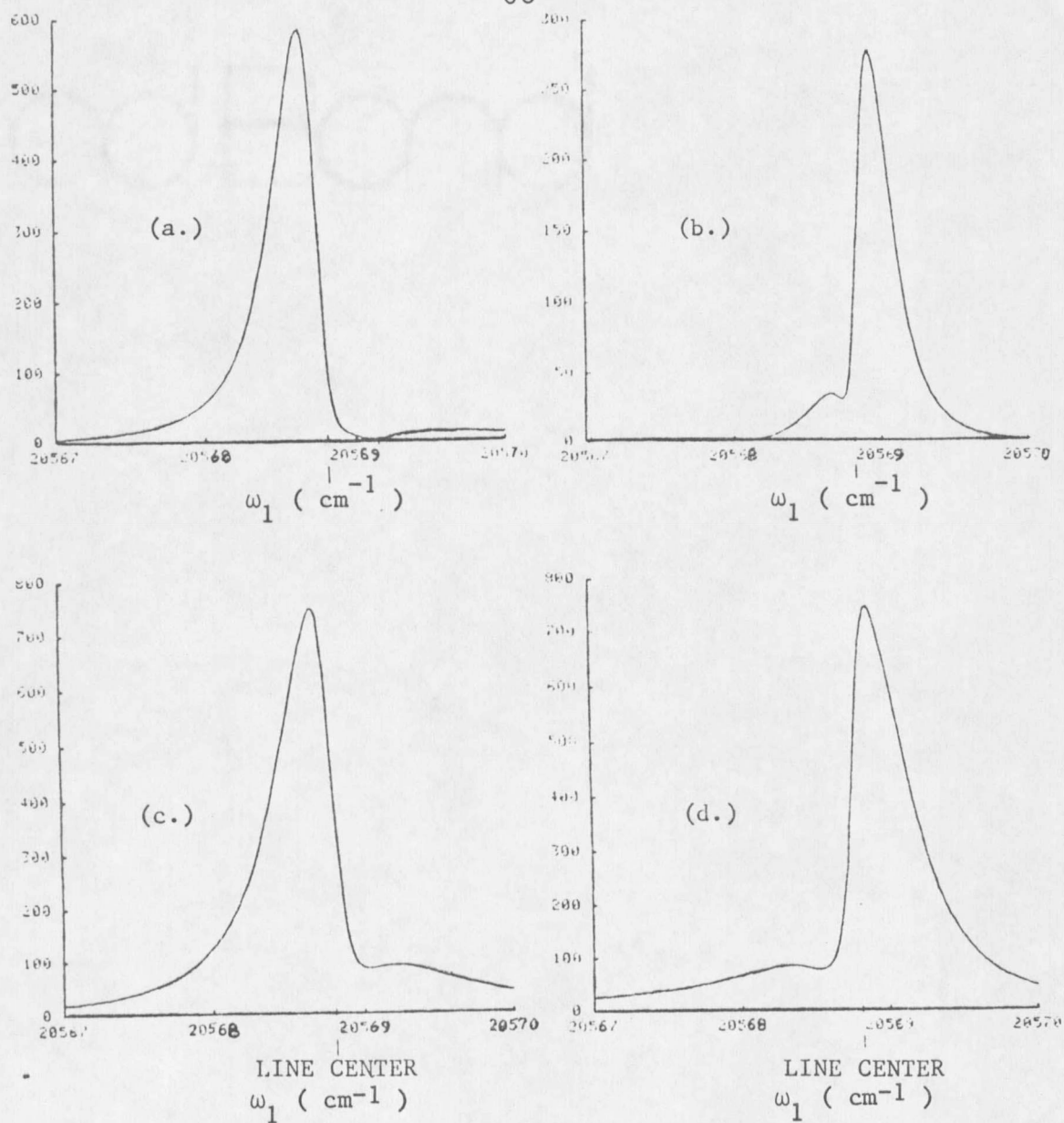


Figure 4.9. Computer simulation of equation 4.1 for 4 different crossing angles. (a.) $\theta = 1.25^\circ$, (b.) $\theta = 3.0^\circ$, (c.) $\theta = 1.75^\circ$, and (d.) $\theta = 2.5^\circ$.

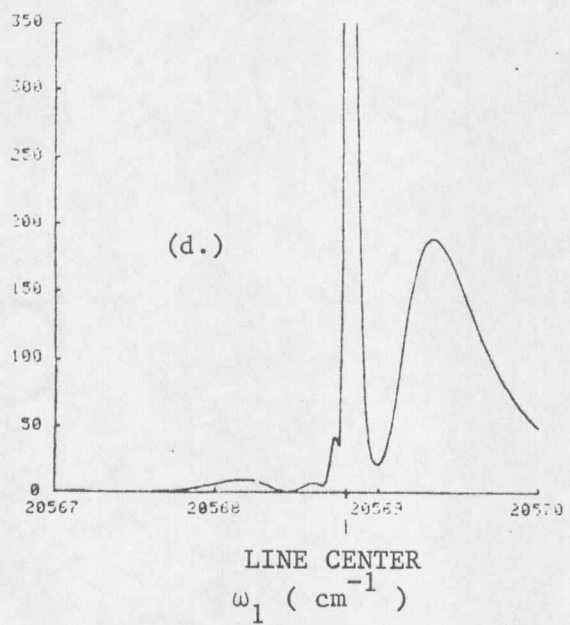
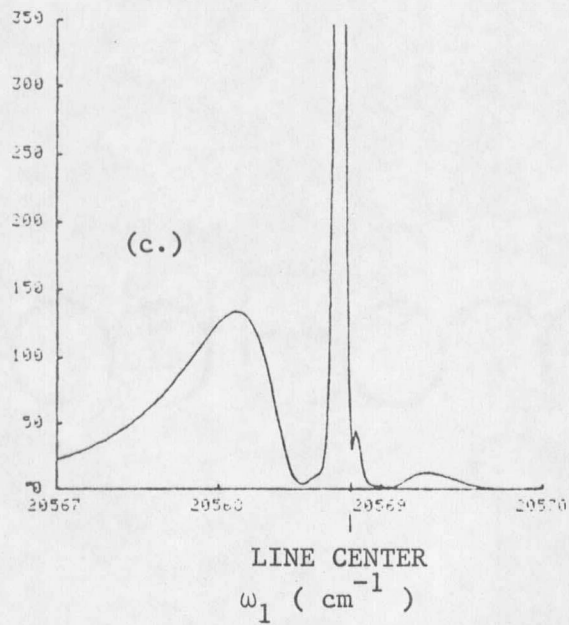
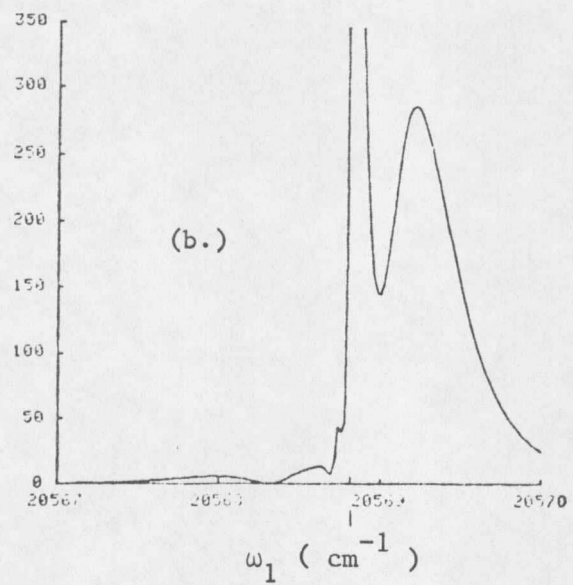
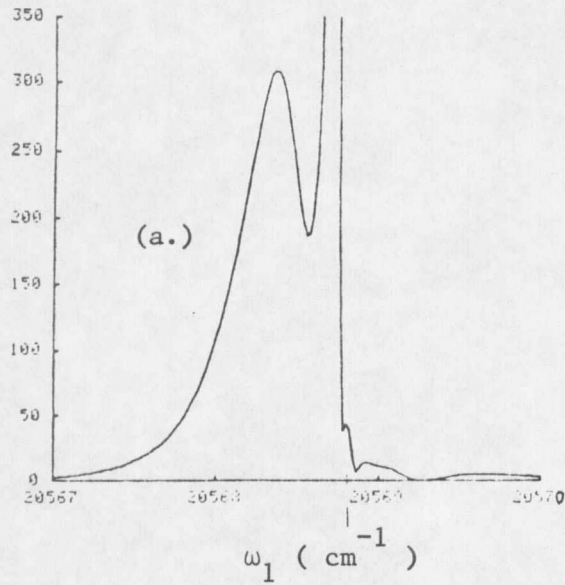


Figure 4.10. Computer simulation of equation 4.1 with Δn increased by 3.8. (a.) $\theta = 0.0^\circ$, (b.) $\theta = 3.3^\circ$, (c.) $\theta = 1.5^\circ$, (d.) $\theta = 2.8^\circ$.

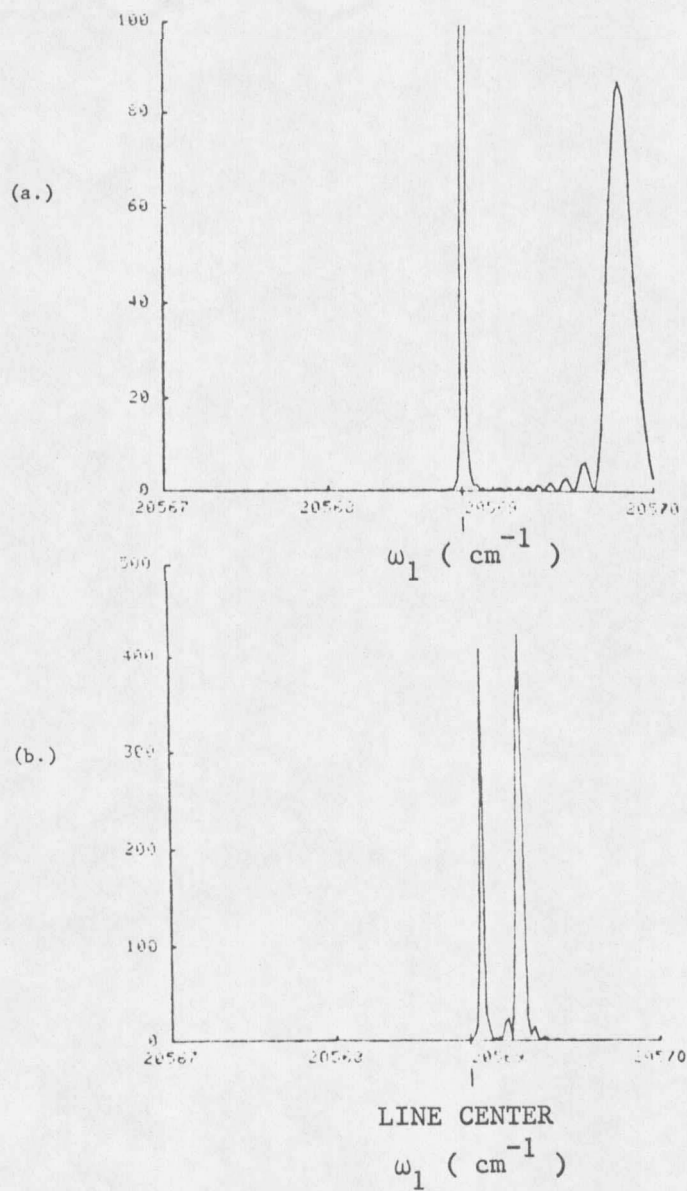


Figure 4.11. Computer simulation of equation 4.1 with Δn increased 35 times. (a.) $\theta = 5.5^\circ$, and (b.) $\theta = 8.0^\circ$.

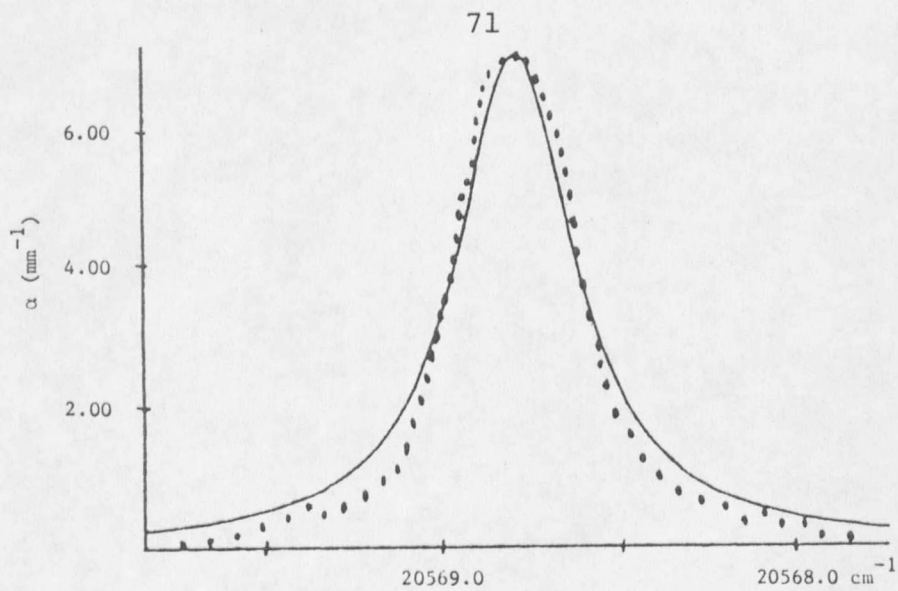


Figure 4.12. Lorentzian profile fitted to white-light absorption coefficient. Data given by • .

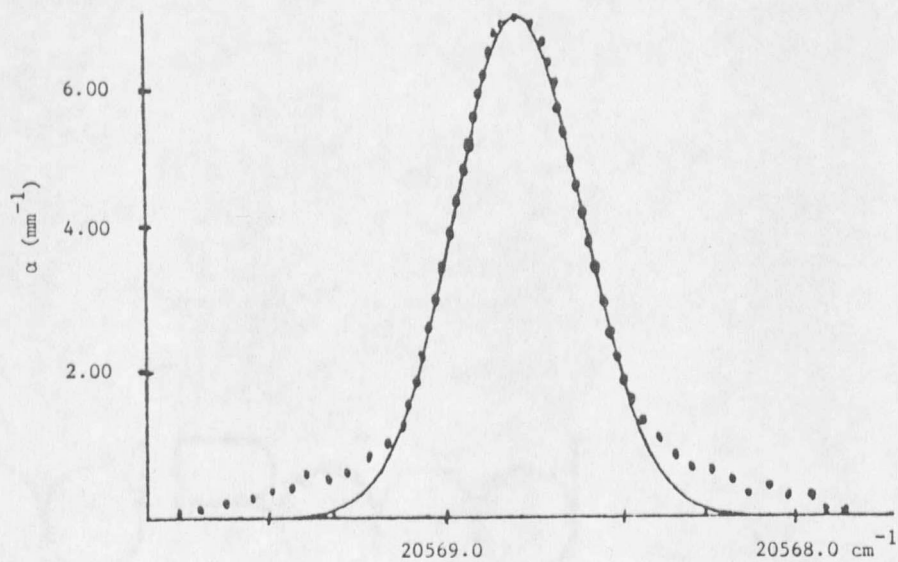


Figure 4.13. Gaussian profile fitted to white-light absorptions coefficient. Data given by • .

4.6 (a) shows that we have approximately a Voigt profile (which has a Gaussian center and Lorentzian wings) rather than the pure Lorentzian used in the simulation.

To more realistically describe the inhomogeneously broadened line shape, the complex plasma dispersion function⁷⁴ can be used which incorporates the broadened index and absorption functions as its real and imaginary parts. It requires numerical integration but could otherwise be easily worked into the model and may give closer fits.

Note also that the four-wave mixing signal was never experimentally observed near line center even though several intermediate values of θ were tried. Furthermore, as the ω_4 signal moved in that direction, a decrease in intensity was observed. (The scans presented in Figure 4.5 are not all on the same vertical scale.) Several possibilities could account for this.

Saturation effects, assumed negligible in Chapter 2, could inhibit signal intensity through factors of the type $\Delta N_{ij} \equiv \rho_{ii} - \rho_{jj}$ associated with each term^{18,75} of the nonlinear susceptibility. Saturation occurs when $\Delta N_{ij} \rightarrow 0$, reducing the source polarization and therefore the signal. However, we calculate in Appendix III that saturation is

negligible indicating this is an unlikely explanation.

A second possibility can be seen by examining the spectral width of the lines shown in Figure 4.9 (spectra generated with large index). Note that the line phase matched on the steep inside portion of the index curve is narrower than the laser linewidth, therefore it uses only a fraction of the laser power available for signal generation. As a result, it would become too weak for detection.

The most interesting possibility, however, is the following. Because the narrowing is a coherence effect, a phase matching window less than the homogeneous linewidth ought to severely depress the signal. If this is true, the homogeneous linewidth becomes a fundamental limit of phase matching induced line narrowing.

We have reason to believe that such may be the case here. The splitting observed in the fluorescence excitation of both compounds is related to exciton annihilation which increases the width of the homogeneous packets near line center. As discussed in Chapter 2, exciton annihilation is a cooperative process that arises when neighboring excited ions transfer energy from one to the other. This drops one of the ions into a lower state while further exciting the

other one. Thus two ions are nonradiatively removed from the fluorescing state.

The probability for this to occur is a strong function of excitation density which depends upon position within the absorption lineshape. As the laser scans onto line center, the excitation density becomes higher, enhancing this process, quenching the 5D_4 fluorescence, and creating a hole in the spectrum. (See Appendix IV for experimental aspects of fluorescent light collection, which are also relevant to the interpretation of the splitting.)

The rapid depopulation of the 5D_4 state associated with the annihilation will broaden the homogeneous line width to a greater degree on line center than on the wings. When the homogeneous broadening becomes greater than the phase matching window (which is narrowest at line center), signal strength ought to decrease.

The narrowest line observed in $Tb(OH)_3$ was 0.22 cm^{-1} wide on the $\mu = 3^+$ state (Figure 4.12 (a)). This is significantly greater than the 0.056 cm^{-1} (Figure 1.1b) of $LiTbF_4$ measured under similar conditions. We are thus being limited by either the index slope or the homogeneous line-width. Whichever is the case, it implies a dephasing time

$T_2 \equiv \frac{1}{\hbar\Delta\nu} \geq 50$ psec. Chen and Meltzer⁴⁷ also obtained this value for the nearby $\mu = 2$ state by studying its time-resolved band-to-band exciton emission. Confirmation of this hypothesis could be made using photon echo techniques, however, the picosecond relaxation times involved are beyond the current state of the art for coherent transient measurements.

Applications

The most obvious application of this technique is in using the spectral narrowing to measure homogeneous linewidths of strain-broadened lines. This ought to have much wider application than other techniques relying on polarization tricks, special resonances, or collision-induced narrowing effects. Assuming our interpretation is correct and experimental parameters such as sample length, focusing conditions, laser power, and laser bandwidth are properly controlled, the signal linewidth is limited only by the slope of the index or the homogeneous linewidth. In materials with rapid dephasing, the homogeneous linewidth will be the limiting factor.

A second application is in UV and VUV spectroscopy.

This was already demonstrated in our two-photon resonance experiment which resolved a narrow crystal field component from the broad $4f^75d$ absorption band seen in the linear absorption. It showed resonant enhancement of over twenty-five times.

Because TPAFWM uses different selection rules than linear absorption, it ought to provide new information on UV levels in previously unexplored spectral regions and aid in their identification. Knowledge of these levels is essential in evaluation of the assumptions made in the Judd-Ofelt parameterization scheme mentioned in Chapter 2. Furthermore, the presence of the intermediate state allows transitions from it to UV levels to be studied. Linear methods do not provide this information.

Experimentally, the chief advantage of TPAFWM over linear absorption methods lies in its ability to explore the UV and VUV using visible laser beams. This allows the use of conventional lasers, optics, and detection systems designed for use in the visible region of the spectrum.

A third application involves coherent transient measurements. They enable T_2 to be measured directly. These kinds of experiments are especially useful in those

cases where spectral lines are narrower than available laser linewidths. They thus complement frequency domain measurements. Appendix I describes in detail the coherent transient technique that would be associated with the TPAFWM process.

Chapter 5

CONCLUSIONS

A new type of four-wave mixing spectroscopy, involving both single and two-photon resonances, has been developed which holds promise in two major areas: dynamical measurements of excited states, and UV and VUV spectroscopy.

Upon application of three laser beams of frequencies ω_1 , ω_2 , and ω_3 to crystalline samples of both $\text{Tb}(\text{OH})_3$ and LiTbF_4 , a doubly-resonant two-photon-absorption-induced four-wave mixing (TPAFWM) signal at frequency $\omega_4 = \omega_1 + \omega_2 - \omega_3$ was produced. The nature of the signal was decided from its temporal, power, frequency, and polarization dependence along with direct measurement of both resonances.

The ω_4 signal exhibited spectral selectivity and, under appropriate conditions, laser-limited linewidths ten times narrower than the inhomogeneous width of the intermediate state. This was qualitatively explained as arising from the dispersive nature of the index of refraction and its effect on phase matching. This was the first such narrowing seen in any system. It is an effect which will need to be considered in all resonant four-wave mixing

experiments.

A direct measurement of the linear anomalous index of refraction was made using a prism-shaped sample of LiTbF_4 . This measurement, along with the measured inhomogeneous white-light absorption, provided the necessary parameters to quantitatively check the model.

The results obtained gave qualitative but not quantitative fits to the data. To resolve the situation we assumed contribution of the nonlinear index to the phase matching. We further correlated observed exciton annihilation at line center to the loss of four-wave mixing signal in the same region.

For materials with rapid dephasing, the narrowing may ultimately be limited by the homogeneous linewidth. If this is the case, such measurements would provide important information on the dynamics of excited states. For $\text{Tb}(\text{OH})_3$, this would indicate a lower bound of $T_2 \geq 50$ psec.

An additional application of this technique involves the spectroscopy of UV and VUV levels. This was demonstrated in the measurement of a 230 cm^{-1} wide crystal field component of the $4f^7 5d$ configuration in $\text{Tb}(\text{OH})_3$.

The chief advantages of this method over linear techniques are: (a) the two-photon nature of the mixing

uses different selection rules than linear UV absorption, allowing complementary information to be obtained, (b) the intermediate state resonance provides the ability to study transitions between excited states, and (c) UV and VUV spectroscopy can be done using visible lasers, optics, and detection systems.

Finally, coherent transient measurements were discussed. Use of transform-limited pulses ought to allow this technique to become a powerful method complementing frequency domain spectroscopy.

As is usual in scientific endeavor, efforts to answer one question often open up new areas of exploration. In this case, they include not only understanding the finer details of the narrowing but also using the technique as an investigative tool in such areas as excited state dynamics and UV spectroscopy.

One experiment would involve measuring the power dependence of the index of refraction and comparing it to the expected power dependence of the phase matching selectivity and narrowing. This would tell us to what degree the nonlinear refractive index is contributing to the phase matching conditions.

The one disadvantage to the index wedge experiment was that it could not be performed with power densities such as those used in mixing. Highly collimated beams and therefore large waists were necessary to avoid diffraction effects so that we could accurately measure the index changes.

An alternative to the wedge experiment involving polarization tricks⁷⁶ may be used. By placing the crystal between crossed polarizers, one can map out the real part of the index while scanning through resonance. Although beam collimation is important here, as well, it is less restrictive. Preliminary experiments on $\text{Tb}(\text{OH})_3$ have been performed indicating the feasibility of this technique.

Four-wave mixing experiments using more monochromatic lasers need to be done. Laser linewidth could be the limiting factor in the LiTbF_4 measurement where the narrowest signal recorded was 0.056 cm^{-1} .

Four-wave mixing experiments need to be tried on other crystals. Use of three input beams allows greater flexibility in matching wavelengths to transitions. The excited $4f^{n-1}5d$ configuration energies are greater in most other trivalent rare earths, therefore one of the lasers would need a frequency doubled output in order for the ex-

cited configuration to be reached. It would be interesting to try FWM in Nd:YAG since this is a well known laser material.

If transform-limited pulsed lasers could be used, coherent transient FWM measurements could be done on various Eu compounds. Macfarlane has already measured $T_2 = 20 \mu\text{sec}$ using a photon echo technique⁷⁷ in $\text{EuP}_5\text{O}_{14}$. $\text{Eu}(\text{OH})_3$, with a measured inhomogeneous width of ~ 200 MHz,⁷⁸ could possibly have a dephasing time on the order of nanoseconds. Use of other kinds of coherent transient techniques on the same crystals would provide a baseline from which to compare FWM data.

Finally, it would be interesting to try the FWM experiment at room temperature. Most crystal systems would be homogeneously broadened to the point where phase matching selectivity is lost. However, if selectivity and narrowing were seen, it would have significant impact especially with the high interest in degenerate four-wave mixing for device applications.

APPENDICES

APPENDIX I

APPENDIX I

COHERENT TRANSIENT MEASUREMENTS

Coherent transient techniques^{13,34} provide a powerful way to directly measure the dephasing (phase relaxation) time, T_2 , of an induced collective dipole moment of a material system. As mentioned in Chapter 1, photon echo^{35,36} experiments allow measurement of the homogeneous T_2 for inhomogeneously broadened lines. In contrast, FWM methods only yield correct measurements of T_2 in systems where homogeneous broadening dominates. (This will be explained later.)

We will show here that, FWM techniques ought to be useful on inhomogeneously broadened lines (assuming a homogeneous limit to the narrowing as argued in Chapter 4.) This would have distinct advantages over photon echo methods such as spatial and frequency discrimination of the signal as well as the ability to measure T_2 associated with states of large energy separation (even into the UV). The FWM method should work for both TPAFWM and coherent resonant Raman¹⁵ transient techniques.

The basic FWM experiment is performed as follows. We consider the case of doubly-resonant TPAFWM as in

Chapter 4. Three laser beams of frequencies ω_1 , ω_2 , and ω_3 are crossed inside the crystal at an internal angle that gives the narrowest linewidth (presumably the homogeneous linewidth). The frequencies are resonant with the energy levels shown in Figure I.1.

In order to measure the dipole decay of ρ_{ab} , the sequence of pulses illustrated in Figure I.2 is applied. We will show that the intensity of the generated ω_4 signal will be exponentially related to the decay over time delay T of the coherence induced by the laser pulse at ω_1 .

We assume a four level system and, using the notation of Andrews and Hochstrasser,⁷⁹ allow population decay with rates γ_{da} , γ_{db} , γ_{dc} , γ_{ca} , γ_{cb} , and γ_{ba} as illustrated in Figure I.1. A population reservoir is included as well to allow for decay to levels other than the four explicitly shown. Decay into the reservoir from the four levels occurs with rates γ_{dr} , γ_{cr} , γ_{br} , and γ_{ar} . The reservoir can feed state $|a\rangle$ at the rate γ_{ra} .

We have for the density matrix equation of motion in the Schrodinger picture,

$$\dot{\rho} = -(i/\hbar) [H_0, \rho] - (i/\hbar) [V, \rho] + \dot{\rho}_{\text{relax}} \quad (\text{I.1})$$

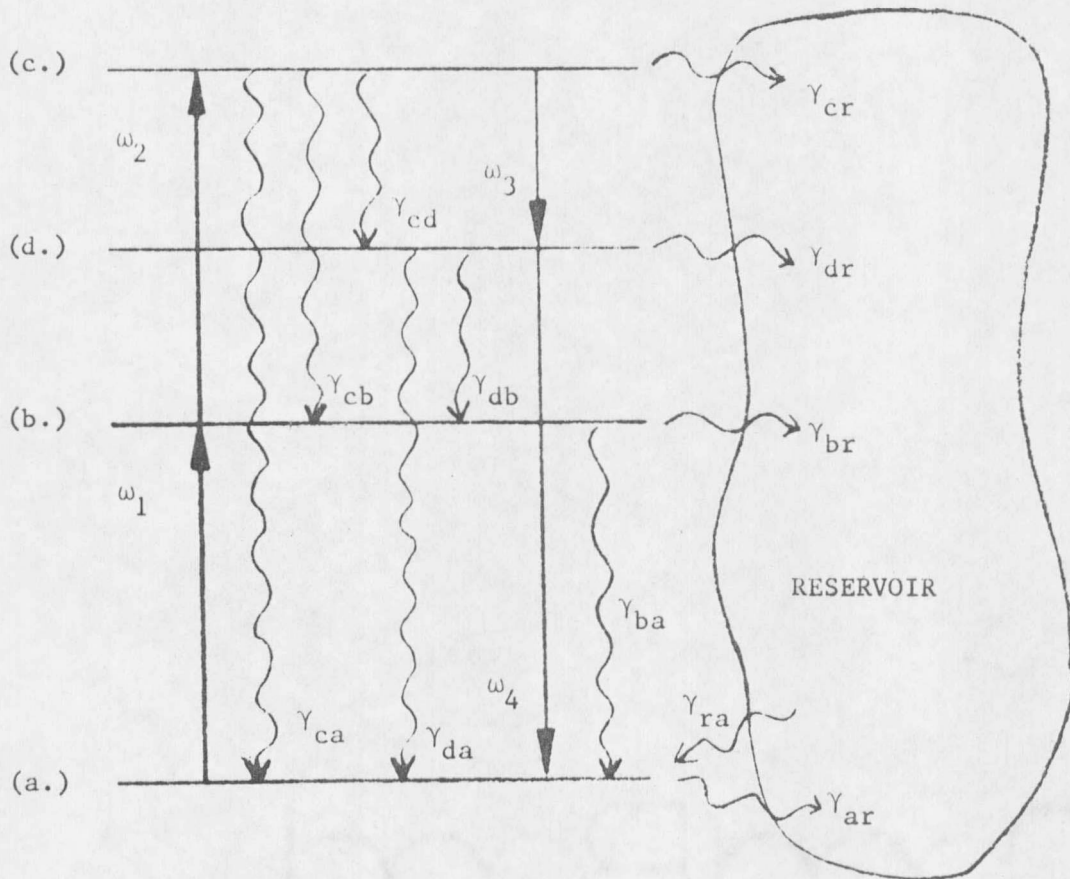


Figure I.1. Four level system with reservoir.

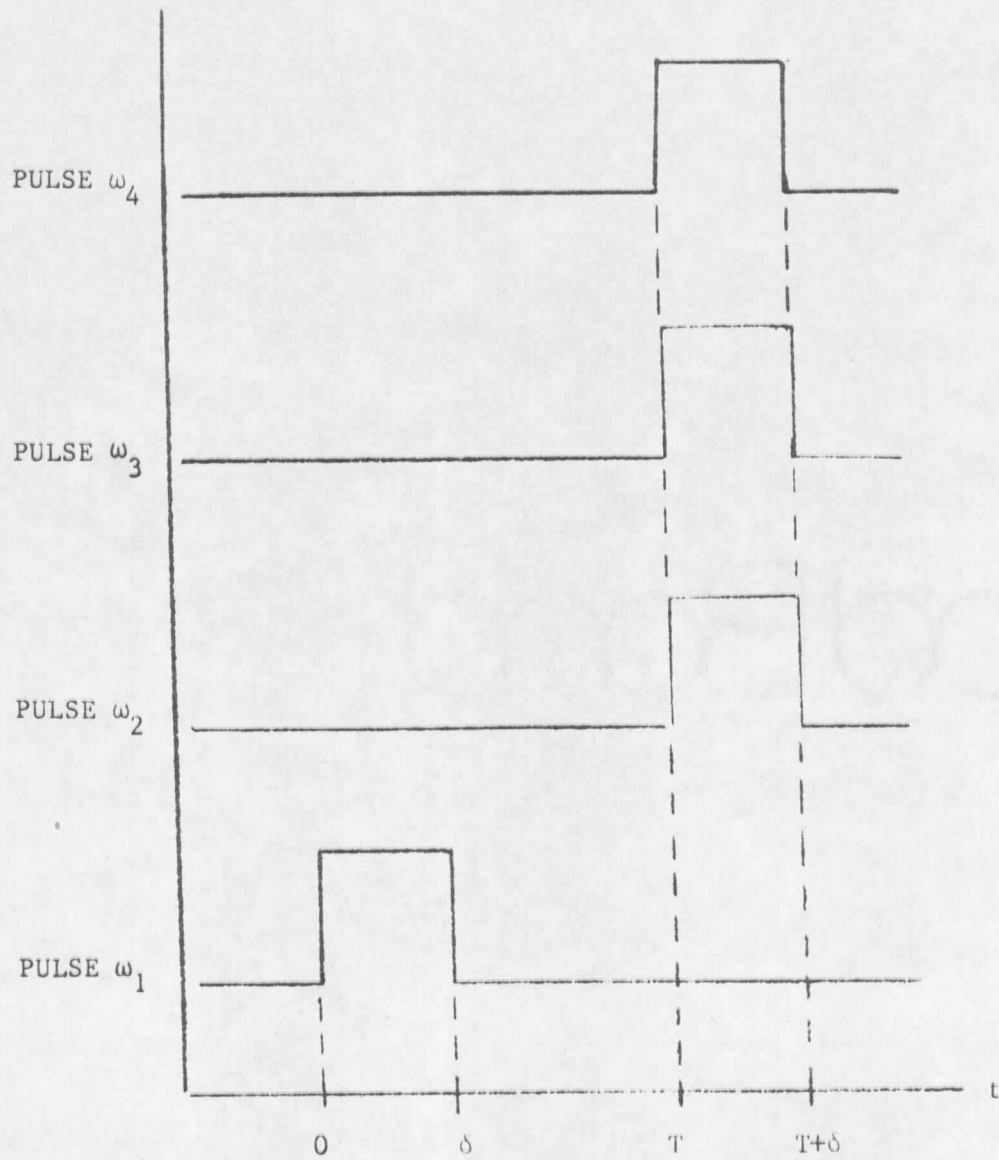


Figure I.2. Temporal sequence of laser pulses in 3-beam coherent transient experiment.

where $(\dot{\rho}_{\text{relax}})_{nn'} = -\Gamma_{nn'} \rho_{nn'}$ (I.2)

$$(\dot{\rho}_{\text{relax}})_{nn} = -\sum_n \gamma_{nn} \rho_{nn} + \sum_n \gamma_{n'n} \rho_{n'n'}$$

and $V(t) = -\vec{\mu} \cdot \vec{E}(t)$. Note that Andrews defines

$\gamma_{nn'}$ as $\gamma_{n'n}$ used in Chapter 2.

Applying these equations to our four level system we obtain ten coupled differential equations:

$$\begin{aligned} \dot{\rho}_{aa} = & -\gamma_{ar} \rho_{aa} + \gamma_{da} \rho_{dd} + \gamma_{ca} \rho_{cc} + \gamma_{ba} \rho_{bb} + \gamma_{ra} (\rho_{bb} + \rho_{cc} + \rho_{dd}) \\ & - (i/\hbar) (V_{ab} \rho_{ba} - \rho_{ab} V_{ba} + V_{ad} \rho_{da} - \rho_{ad} V_{da} + V_{ac} \rho_{ca} - \rho_{ac} V_{ca}) \end{aligned} \quad (\text{I.4a})$$

$$\begin{aligned} \dot{\rho}_{bb} = & -(\gamma_{br} + \gamma_{ba}) \rho_{bb} + \gamma_{db} \rho_{dd} + \gamma_{cb} \rho_{cc} - (i/\hbar) (V_{ba} \rho_{ab} - \rho_{ba} V_{ab} \\ & + V_{bd} \rho_{db} - \rho_{bd} V_{db} + V_{bc} \rho_{cb} - \rho_{bc} V_{cb}) \end{aligned} \quad (\text{I.4b})$$

$$\begin{aligned} \dot{\rho}_{dd} = & -(\gamma_{dr} + \gamma_{da} + \gamma_{db}) \rho_{dd} + \gamma_{cd} \rho_{cc} - (i/\hbar) (V_{da} \rho_{ad} - \rho_{da} V_{ad} \\ & + V_{db} \rho_{bd} - \rho_{db} V_{bd} + V_{dc} \rho_{cd} - \rho_{dc} V_{cd}) \end{aligned} \quad (\text{I.4c})$$

$$\begin{aligned} \dot{\rho}_{cc} = & -(\gamma_{cr} + \gamma_{ca} + \gamma_{cb} + \gamma_{cd}) \rho_{cc} - (i/\hbar) (V_{ca} \rho_{ac} - \rho_{ca} V_{ac} \\ & + V_{cb} \rho_{bc} - \rho_{cb} V_{bc} + V_{cd} \rho_{dc} - \rho_{cd} V_{dc}) \end{aligned} \quad (\text{I.4d})$$

$$\begin{aligned} \dot{\rho}_{ab} = & (i\omega_{ba} - \Gamma_{ab})\rho_{ab} - (i/\hbar)(V_{ab}(\rho_{bb} - \rho_{aa}) \\ & + V_{ad}\rho_{db} - \rho_{ad}V_{db} + V_{ac}\rho_{cb} - \rho_{ac}V_{cb}) \end{aligned} \quad (\text{I.4e})$$

$$\begin{aligned} \dot{\rho}_{ad} = & (i\omega_{da} - \Gamma_{ad})\rho_{ad} - (i/\hbar)(V_{ad}(\rho_{dd} - \rho_{aa}) \\ & + V_{ab}\rho_{bd} - \rho_{ab}V_{bd} + V_{ac}\rho_{cd} - \rho_{ac}V_{cd}) \end{aligned} \quad (\text{I.4f})$$

$$\begin{aligned} \dot{\rho}_{ac} = & (i\omega_{ca} - \Gamma_{ac})\rho_{ac} - (i/\hbar)(V_{ac}(\rho_{cc} - \rho_{aa}) \\ & + V_{ab}\rho_{bc} - \rho_{ab}V_{bc} + V_{ad}\rho_{dc} - \rho_{ad}V_{dc}) \end{aligned} \quad (\text{I.4g})$$

$$\begin{aligned} \dot{\rho}_{bd} = & (i\omega_{db} - \Gamma_{bd})\rho_{bd} - (i/\hbar)(V_{bd}(\rho_{dd} - \rho_{bb}) \\ & + V_{ba}\rho_{ad} - \rho_{ba}V_{ad} + V_{bc}\rho_{cd} - \rho_{bc}V_{cd}) \end{aligned} \quad (\text{I.4h})$$

$$\begin{aligned} \dot{\rho}_{bc} = & (i\omega_{bc} - \Gamma_{cb})\rho_{bc} - (i/\hbar)(V_{bc}(\rho_{cc} - \rho_{bb}) \\ & + V_{ba}\rho_{ac} - \rho_{ba}V_{ac} + V_{bd}\rho_{dc} - \rho_{bd}V_{dc}) \end{aligned} \quad (\text{I.4i})$$

$$\begin{aligned} \dot{\rho}_{dc} = & (i\omega_{cd} - \Gamma_{dc})\rho_{dc} - (i/\hbar)(V_{dc}(\rho_{cc} - \rho_{dd}) \\ & + V_{da}\rho_{ac} - \rho_{da}V_{ac} + V_{db}\rho_{bc} - \rho_{db}V_{bc}) \end{aligned} \quad (\text{I.4j})$$

where $\omega_{ij} \equiv (\omega_i - \omega_j)$.

As shown in Figure I.2, pulses at frequencies ω_2

and ω_3 are applied T seconds after the end of the ω_1 pulse. The ω_2 and ω_3 pulses interact with the remaining coherence of ρ_{ab} to generate the ω_4 signal.

We assume "square" pulses with width $\delta \ll T, T_2$. We start with the initial conditions $\rho_{aa}(0) = 1$ and $\rho_{ij}(0) = 0$ for all $i, j \neq a$, and use the iterative perturbational approach described in Chapter 2. However, for this case we are interested in the transient solution.

Since we know the resonant behavior of the signal from the experiments described in Chapter 4, we can use this information to pick out the leading terms at $\omega_4 = \omega_1 + \omega_2 - \omega_3$.

The first pulse at ω_1 establishes coherence associated with states $|a\rangle$ and $|b\rangle$. For times $\delta < t < T$, solution of I.4 yields the leading terms:

$$\rho_{aa}^{(0)}(t) + \rho_{aa}^{(1)}(t) = 1$$

and

$$\rho_{ab}^{(1)}(t) = (\text{const.}) \exp [(i\omega_{ba} - \Gamma_{ab})(t-\delta)].$$

At $t = T$, $\rho_{ab}^{(1)}(T)$ provides the initial conditions for the arrival of the delayed pulses at ω_2 and ω_3 . Final

solution for the intensity of the signal at ω_4 involves integration of only one time-ordered term (due to the resonant enhancement of that term relative to the others).

The result is

$$I(\omega_4) \propto \exp[-2\Gamma_{ab}(T-\delta)]$$

for delay T .

Note that, in order to have any temporal resolution, we need $\delta \ll T_2$. This implies using laser bandwidths $\Delta \nu \gg \Gamma_{ab}$ since the width of the homogeneous line (as described in Chapter 2) is $2\Gamma_{ab}$.

However, in an inhomogeneously broadened system, adherence to this condition excites several homogeneous packets thereby increasing the dephasing rate. Thus coherent transient measurements of this type appear to be useless unless some mechanism restricts the interaction to only one homogeneous packet.

If the phase matching induced selectivity is limited by the homogeneous linewidth, it may provide the necessary mechanism. It will spectrally "filter" those Fourier components from the larger laser bandwidth that match the homogeneous width. Thus temporal resolution can be retained

allowing accurate measurement of T_2 for inhomogeneously broadened lines.

APPENDIX II

APPENDIX II

INDEX OF REFRACTION EXPERIMENT

The index of refraction experiment, as mentioned in Chapter 4, was designed to measure the anomalous dispersion of n at 1.3 K while ω_1 scanned through the 5D_4 resonance. A crystal of $LiTbF_4$ was cut and shaped into a 22.7° triangular prism with the triangular top and bottom perpendicular to the vertical c -axis.

Figure II.1 shows the angular deviation, δ ,⁸⁰ of a beam incident on the prism at angle θ_i immersed in a bath of liquid helium of index⁸¹ $n_0 = 1.029$ which is given by

$$\delta = \theta_i + \sin^{-1} [\sin(\alpha) \left(\left(\frac{n}{n_0} \right)^2 - \sin^2(\theta_i) \right)^{\frac{1}{2}} - \sin(\theta_i) \cos(\alpha)] - \alpha \quad (\text{II.1})$$

where $\alpha = 22.7^\circ$ and, under the condition of minimum deviation, $\theta_i = 17^\circ$. (Minimum deviation occurs for that value of θ_i that minimizes δ . Under this condition, any distortion of the beam spot due to lack of collimation is kept to a minimum.) For⁸² polarized light, n at line center⁸² is 1.508.

Using this information we can calculate the

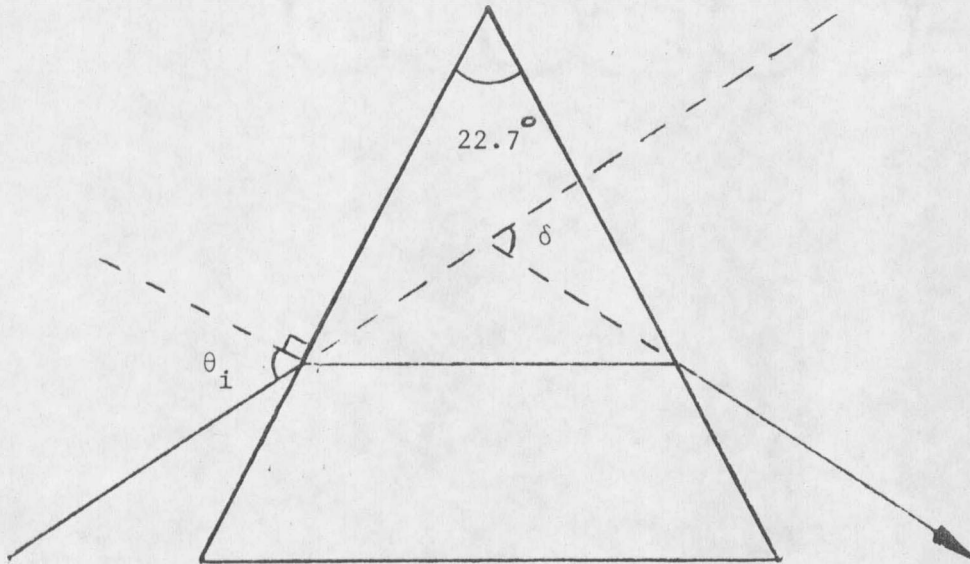


Figure II.1. Angular deviation of beam, δ , traversing LiTbF_6 prism in index of refraction experiment. At minimum deviation, beam path through crystal is parallel to its base.

angular change in beam deviation due to a change in index as ω_1 scans through resonance. We obtain

$$d\delta = 0.40 \, dn \quad (\text{II.2})$$

Therefore by measuring the beam sweep $d\delta$, we can calculate dn .

Because the dispersion was expected to be small, diffraction effects had to be minimized. Thus, the spot size of the beam inside the crystal was $1\frac{1}{2}$ mm which was the largest that could be obtained given the available crystal. This gave a diffraction limit for $d\delta$ of ~ 0.2 mrad.

By placing a weak focusing lens centered on the beam directly outside the exit window of the Dewar, the projected spot (or final beam waist) could be focused without significantly focusing the beam sweep. Using Gaussian beam formulas, a lens of 133 cm was chosen to focus the beam into a minimum waist size while keeping the waist position at a maximum distance from the Dewar. Thus the largest ratio of beam sweep to waist size was obtained.

At the final waist position given by the above lens, an 80 μm translatable slit was placed. Behind the slit, a photo diode detected the light. Diffusers were

placed between the diode and the slit to make the detector insensitive to the beam movement. Measurements were made by translating the slit to obtain the half-power points and then averaging the two readings to get the beam location. Figure II.2 shows the experimental set-up.

Other considerations involved the effect of the Dewar windows and focusing lens on the beam sweep. Both effects were small enough to lie within the error bars generated by beam fluctuations. Finally, the large diameter of the beam in the crystal with its correspondingly low power density presumably ensured the measurement of only the linear index of refraction.

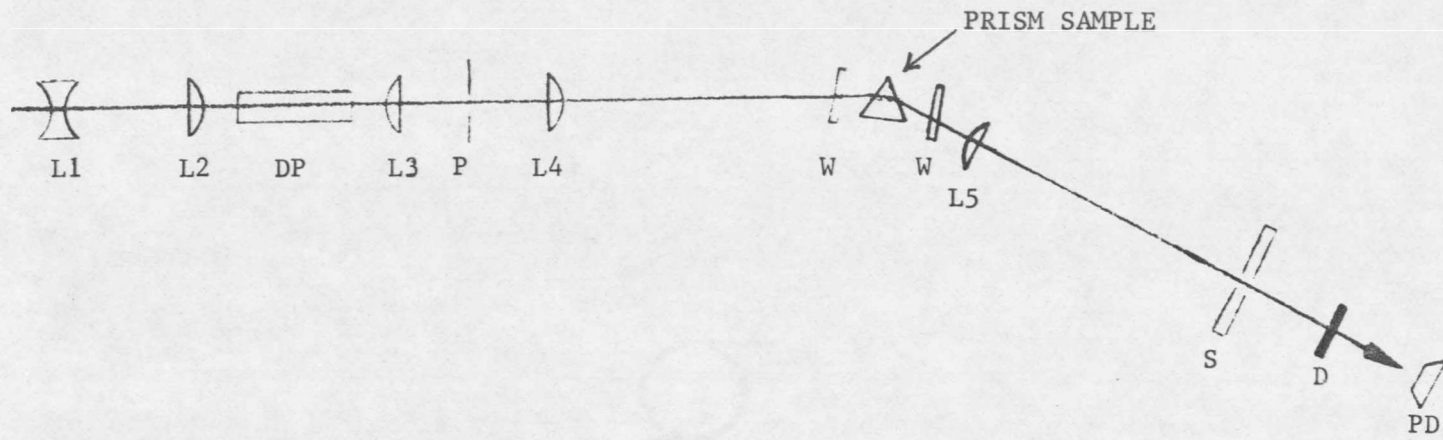


Figure II.2. Experimental set-up for index of refraction experiment.
 Components are the following:

- DP - dispersing prism P - pinhole W - Dewar window(glass Dewar)
- S - 88 μ m slit D - beam diffuser PD - photo diode detector

Beam lenses with focal lengths:

- L1 - -111 cm L2 - 33.3 cm L3 - 13.8 cm
- L4 - 7.5 cm L5 - 133 cm located 1 cm from W.

APPENDIX III

APPENDIX III

SATURATION CALCULATION

As discussed in Chapter 4, saturation effects could play a role in the expression for the third order susceptibility. Thus, we needed to determine if saturation was occurring. A simple calculation illustrates that it is not occurring in the Tb experiments, but that it could in more strongly absorbing samples or at higher laser powers.

Approximately two-thirds of the incident photons are absorbed in a depth of $\alpha^{-1}(\omega_0)$ inside the crystal where $\alpha(\omega_0)$ is the line center absorption coefficient. Using this depth and the beam cross-sectional area, we can define a cylindrical volume to calculate the number density of absorbed photons, \tilde{N} .

From Figure 4.6 (a) we obtain $\alpha^{-1}(\omega_0) \sim 150 \mu\text{m}$.

From the experimental parameters listed below,

Energy per photon at $\omega_1 \sim 4 \times 10^{-19} \text{J}$

Pulse energies $\sim 50 \mu\text{J}$

Beam waist (radius) $\sim 35 \mu\text{m}$

we obtain an excitation density of $\tilde{N} \sim 1.4 \times 10^{20}$ excited ions/cm³.

We calculate the ion density, N_0 , from the molar volume given by Catenese⁶⁶ to be $N_0 = 1.6 \times 10^{22}$ ions/cm³. Since saturation occurs for $N = N_0/2$, we see that it is a negligible affect for the conditions of our experiments.

APPENDIX IV

APPENDIX IV

SPURIOUS SPECTRAL SPLITTINGS

In addition to the exciton annihilation discussed in Chapter 4, the splitting in the fluorescent excitation spectrum of Figure 4.1 (a) also depends upon alignment of the light collection system. This can be explained in the following manner.

For such strongly absorbing compounds as $\text{Tb}(\text{OH})_3$ and LiTbF_4 , the absorption length on resonance is much less than the crystal thickness. (See Figure 4.6 (a) in which the inhomogeneously broadened white-light absorption coefficient obtained with a thinner sample of LiTbF_4 is presented.)

Inside the crystal, the photon density of ω_1 depends upon the number of photons previously absorbed in regions closer to the crystal surface. This is a function of both location inside the crystal and spectral position within the absorption. Thus the decreased photon number in the crystal interior generates less fluorescence than the surface region. This causes spectra collected from the interior to suffer from a "hole" at line center where absorption is strongest. The lateral collection

of light used accentuates this problem. The effect can be minimized by collecting light in a back-scattered geometry.

REFERENCES

REFERENCES

1. R. L. Cone, J. M. Friedman, R. A. Stepnoski, D. A. Ender, M. S. Otteson, and Paula L. Fisher, (Submitted to Phys. Rev. Lett., 1982).
2. D. A. Ender, R. L. Cone, M. S. Otteson, M. B. Ritter, and H. J. Guggenheim, (Submitted to Opt. Lett., 1982).
3. R. L. Cone, D. A. Ender, M. S. Otteson, Paula L. Fisher, J. M. Friedman, and H. J. Guggenheim, in Laser Techniques for Extreme Ultraviolet Spectroscopy, AIP Conference proceedings, March 8-10, 1982.
4. P. A. Franken, A. E. Hill, C. W. Peters, and G. Weinreich, Phys. Rev. Letters 7, 118 (1961).
5. Amnon Yariv, Quantum Electronics, 2nd Edition, (Wiley, New York, 1975), p. 422.
6. Eugene Hecht and Alfred Zajak, Optics, (Addison-Wesley, Reading, Massachusetts, 1975), pp. 263-266.
7. Although Townes, Prokhorov, and Basov won the 1964 Nobel prize for their work in the maser-laser field, Theodore H. Maiman of Hughes Research Labs took the honor of building the first laser: Nature 187, 493 (1960); British Communications and Electronics 1, 674 (1960).
8. Concetto R. Giuliano, Phys. Today 34, (4), 27 (1981).
9. G. B. Lubkin, Phys. Today 34 (12), 17 (1981); N. Bloembergen, Science 216, 1057 (1982), A. L. Schawlow, Science 217, 9 (1982).
10. N. Bloembergen, editor, Proceedings of the International School of Physics Enrico Fermi Course LXIV: Nonlinear Spectroscopy, (North Holland, Amsterdam, 1977); N. Bloembergen, in Laser Spectroscopy IV, edited by H. Walther and K. W. Rothe, (Springer, Berlin, 1979), pp. 340-348. See also Y. R. Shen, Rev. Mod. Phys. 48, 1 (1976).

11. Theodore W. Hänsch, *Phys. Today* 30 (5), 34 (1977).
12. Marc D. Levenson, *Ibid.*, p. 44.
13. Richard G. Brewer, *Ibid.*, p. 50.
14. M. D. Levenson and J. J. Song, in Coherent Nonlinear Optics, edited by M. S. Feld and V. S. Letokov, (Springer-Verlag, Berlin, 1980), pp. 293-372.
15. S. Laubereau and W. Kaiser, *Ibid.*, pp. 271-292; *Rev. of Mod. Phys.*, 50, 608 (1978).
16. Adéibert Owyong, *IEEE J. of Quant. Elect.* QE-14, 192 (1978).
17. B. F. Levine and C. G. Bethea, *IEEE J. of Quant. Elect.* QE-16, 85 (1980).
18. W. M. Tolles, J. W. Nibler, J. R. McDonald, A. B. Harvey, *Appl. Spect.* 31, 253 (1977).
19. J. R. Andrews, and R. M. Hochstrasser, and H.P. Trommsdorff, *Chem. Phys.* 62, 87 (1981).
20. J. R. Andrews, and R. M. Hochstrasser, *Chem. Phys. Lett.* 83, 427 (1981).
21. N. Bloembergen, in Laser Spectroscopy IV, edited by H. Walther and K. W. Rothe, (Springer, Berlin, 1979), pp. 340-348, N. Bloembergen, *Science* 216, 1057 (1982).
22. J. L. Oudar and Y. R. Shen, *Phys. Rev. A* 22, 1141 (1980).
23. N. Bloembergen, H. Lotem, and R. T. Lynch, Jr., *Indian J. Pure Appl. Phys.* 16, 151 (1978).
24. R. L. Abrams and R. C. Lind, *Opt. Lett.* 2, 94 (1978).
25. L. M. Humphrey, J. P. Gordon, and P. F. Liao, *Opt. Lett.* 5, 56 (1980).

26. P. M. Selzer, in Laser Spectroscopy of Solids, edited by W. M. Yen and P. M. Selzer, (Springer-Verlag, Berlin, 1981), pp. 136-137.
27. Amnon Yariv, p. 165-173.
28. T. W. Hänsch, in Nonlinear Spectroscopy, edited by N. Bloembergen, (North-Holland, Amsterdam, 1977), pp. 17-63.
29. P. M. Selzer, pp. 126-129.
30. T. W. Hänsch, in Nonlinear Spectroscopy, pp. 63-83.
31. J. J. Song, J. H. Lee, and M. D. Levenson, Phys. Rev. A 17, 1439 (1978).
32. C. Wieman and T. W. Hänsch, Phys. Rev. Lett. 36, 1170 (1976); M. D. Levenson, R. M. Macfarlane, and R. M. Shelby, Phys. Rev. B 22, 4915 (1980).
33. M. D. Levenson and J. J. Song, pp. 337-342.
34. R. G. Brewer, in Nonlinear Optics, edited by Philip G. Harper and Brian S. Wherrett (Academic Press, London, 1977), pp. 307-364.
35. Douwe A. Wiersma, in Photoselective Chemistry Part 2, edited by Joshua Jortner, Raphael D. Levine, and Stuart A. Rice, (Wiley, New York, 1981), pp. 421-486.
36. R. M. Macfarlane and R. M. Shelby, Optics Comm. 39, 169 (1981).
37. A. Laubereau and W. Kaiser, Rev. of Mod. Phys. 50, 607 (1978).
38. Izo L. Abram, Robin M. Hockstrasser, James E. Kohl, Myron G. Semack, and David White, J. Chem. Phys. 71, 153 (1979).
39. J. Ducuing, in Nonlinear Optics, pp. 11-45; N. Bloembergen, Nonlinear Optics, (W. A. Benjamin, Reading, Mass., 1977), pp. 20-61.

40. J. A. Armstrong, N. Bloembergen, J. Ducuing, and P. S. Pershan, *Phys. Rev.* 127, 1918 (1962).
41. A. Yariv, pp. 418-421.
42. M. O. Levenson, C. Flytzanis, and N. Bloembergen, *Phys. Rev. B* 6, 3962 (1972).
43. N. Bloembergen, M. D. Levenson, and R. T. Lynch, in Optical Properties of Highly Transparent Solids, edited by S. S. Mitra and B. Bendow (Plenum, New York, 1975), pp. 329-337.
44. A. E. Siegman, An Introduction to Lasers and Masers, (McGraw-Hill, New York, 1971), pp. 304-321.
45. Gary C. Bjorklund, *IEEE J. of Quant. Elect.* QE-11, 287 (1975); W. M. Shaub, A. B. Harvey, and G. C. Bjorklund, *J. of Chem. Phys.* 67, 2547 (1977).
46. R. L. Cone and R. S. Meltzer, *J. of Chem. Phys.* 62, 3573 (1975); R. S. Meltzer and R. L. Cone, *J. of Lumin.* 12/13, 247 (1976); R. S. Meltzer, *Solid State Commun.* 20, 553 (1976).
47. N. T. Chen and R. S. Meltzer, *Phys. Rev. Lett.* 44, 599 (1980).
48. B. G. Wybourne, Spectroscopic Properties of Rare Earths, (Wiley, New York, 1965).
49. S. Hufner, Optical Spectra of Transparent Rare Earth Compounds, (Academic, New York, 1978).
50. Gerhard Dieke, in Spectra and Energy Levels of Rare Earth Ions in Crystals, edited by H. M. Crosswhite and Hanna Crosswhite (Interscience, New York, 1968).
51. Philip D. Scott, PhD. thesis, Yale University, 1970.
52. Another convention used is to label the wave function by the Russell-Saunders symbol used when the spin-orbit interaction becomes negligible.

53. Gerhard Dieke, pp. 82-103.
54. H. P. Christensen, Phys. Rev. B 17, 4060 (1978).
55. S. Hüfner, pp. 98-103.
56. Amnon Yariv, pp. 165-167.
57. D. L. Dexter and R. S. Knox, Excitons, (Interscience, New York, 1965).
58. D. A. Ender, R. L. Cone, and M. S. Otteson, to be published.
59. W. M. Yen and P. M. Selzer, in Lazer Spectroscopy of Solids, edited by W. M. Yen and P. M. Selzer, (Springer-Verlag, Berlin, 1981), pp. 142-188.
60. Two-step absorption is measured by observing the absorption of one laser beam after initial excitation of the 5D_4 level by a different laser beam.
61. Murray Sargent III, Marlan O. Scully, and Willis E. Lamb, Jr., Laser Physics, (Addison-Wesley, Reading, Mass., 1974), pp. 25-27.
62. Eugene Hecht and Alfred Zajak, pp. 307-309.
63. R. Wallenstein and T. W. Hänsch, Opt. Comm. 14, 353 (1975).
64. Philip D. Scott, pp. 1.2-1.3.
65. P. D. Scott, H. E. Meissner, and H. M. Crosswhite, Phys. Lett. 28A, 489 (1969).
66. P. D. Scott and W. P. Wolk, F. of Appl. Phys. 40, 1031 (1969); R. Faulhaber and P. D. Scott, Z. Physik 242, 400 (1971); and C. A. Cateneese, A. J. Skjeltop, H. E. Meissner, and W. P. Wolk, Phys. Rev. B 8, 4223 (1973).

67. L. M. Holmes, J. Als-Nielsen, and H. J. Guggenheim, Phys. Rev. B 12, 180 (1975).
68. H. P. Christensen, Phys. Rev. B 17, 4060 (1978).
69. J. L. Oudar, A. Maruani, E. Batifol, and D. S. Chemla, J. Opt. Soc. Am. 68, 11 (1978).
70. Christos Flytzanis, in Quantum Electronics, Volume I, Nonlinear Optics, Part A, edited by Herbert Rabin and C. L. Tang, (Academic Press, New York, 1975), pp. 9-208.
71. Weak $4f^8 - 4f^8$ transitions may be masked by the strong $4f^7 5d$ absorption in the UV spectrum.
72. The experiment was performed by picking an ω_2 , adjusting the beam crossing angles to achieve comparable phase matching conditions, and then scanning ω_1 through resonance to obtain the peak ω_4 signal intensity. In this manner, a point-by-point measure of the two photon crystal field component used in the FWM was made.
73. L. M. Humphrey, J. P. Gordon, and P. F. Liao, Opt. Lett. 5, 56 (1980); T. Yajima, H. Souma, and Y. Ishida, Phys. Rev. A 17, 324 (1978); J. J. Song, J. H. Lee, and M. D. Levenson, Phys. Rev. A 17, 1439 (1978); J. R. Andrews and R. M. Hochstrasser, Proc. Natl. Acad. Sci. USA 77, 3110 (1980); Y. Prior, A. R. Bogdan, M. Dagenais, and N. Bloembergen, Phys. Rev. Lett. 46, 111 (1981); J. R. Andrews and R. M. Hochstrasser, Chem. Phys. Lett. 83, 427 (1981).
74. Murray Sargent III, Marlan O. Scully, and Willis E. Lamb, Jr., pp. 372-375.
75. S. A. J. Druet, B. Attal, T. K. Gustafson, and J. P. Taran, Phys. Rev. A 18, 1529 (1978).
76. M. D. Levenson, R. M. Macfarlane, and R. M. Shelby, Phys. Rev. B 22, 4915 (1980).

77. R. M. Shelby and R. M. Macfarlane, Phys. Rev. Lett. 45, 1098 (1980).
78. Michael S. Otteson (private communication); This is the narrowest inhomogeneous width of a solid measured to date. A linear spectroscopic method was used.
79. John R. Andrews and Robin M. Hochstrasser, Proc. Natl. Acad. Sci. USA 77, 3110 (1980).
80. Eugene Hecht and Alfred Zajak, pp. 129-131.
81. M. H. Edwards, Can. J. of Phys. 36, 884 (1958).
82. M. J. Weber, R. Morgret, S. Y. Leung, J. A. Griffin, D. Gable, and A. Linz, J. of Appl. Phys. 49, 3464 (1978).

MONTANA STATE UNIVERSITY LIBRARIES
stks D378.En21@Theses RL
Doubly-resonant two-photon-absorption-in



3 1762 00169282 9



D378
En21
Cap 2